Organic sulfur fluxes and geomorphic control of sulfur isotope ratios in rivers

Preston C. Kemeny [a,*], Mark A. Torres [b], Michael P. Lamb [a], Samuel M. Webb [c], Nathan Dalleska [a], Trevor Cole [b], Yi Hou [b], Jared Marske [a], Jess F. Adkins [a], Woodward W. Fischer [a]

[a] *Geological and Planetary Sciences, California Institute of Technology, Pasadena, CA, United States of America*
[b] *Earth, Environmental, and Planetary Sciences, Rice University, Houston, TX, United States of America*
[c] *Stanford Synchrotron Radiation Lightsource, SLAC National Accelerator Laboratory, Menlo Park, CA, United States of America*

ARTICLE INFO

Article history:
Received 28 August 2020
Received in revised form 2 February 2021
Accepted 16 February 2021
Available online 4 March 2021
Editor: L. Derry

Keywords:
chemical weathering
pyrite oxidation
sulfur isotopes
XANES
Iceland

ABSTRACT

Pyrite oxidation plays a critical role in the relationship between weathering and climate, and its impact on the global carbon cycle has previously been constrained through inversion models utilizing observations of river sulfate (SO_4^{2-}) and its $^{34}S/^{32}S$ isotope ratio ($\delta^{34}S_{SO4}$). However, measurements from some rivers have suggested that $\delta^{34}S_{SO4}$ can be substantially impacted by processes such as microbial sulfate reduction and/or sulfur assimilation and cycling, rather than simply reflecting a weighted mixture of lithologic sulfur sources. To study the prevalence and controls on SO_4^{2-} transformations, we measured dissolved major element concentrations and $\delta^{34}S_{SO4}$ in river water samples from throughout western Iceland. Our analyses focused on samples from a small catchment hosting the Efri Haukadalsá river, a system with relatively uniform and isotopically constrained basaltic bedrock. We also measured sediment $\delta^{34}S$ and sulfur speciation using sulfur K-edge X-ray absorption spectroscopy on sediment and vegetation samples from this catchment. Values of dissolved $\delta^{34}S_{SO4}$ in the Efri Haukadalsá ranged from 2.5‰ to 23.7‰ and had a linear relationship with Cl^-/SO_4^{2-} ratios, indicating that SO_4^{2-} predominantly derived from basalt weathering and meteoric precipitation. The lower $\delta^{34}S_{SO4}$ values were found in fluvial valleys with V-shaped cross sections, while higher values of $\delta^{34}S_{SO4}$ occurred in U-shaped, glacially eroded valleys with thick alluvial fills blanketing the valley floor. Spectroscopic observations identified organic sulfur phases in suspended river sediment, floodplain deposits, and vegetation. Mass balance calculations quantified the organic sulfur flux as less than 10% of SO_4^{2-} export, and sediment $\delta^{34}S$ values were comparable to river $\delta^{34}S_{SO4}$. We interpreted these isotopic and chemical patterns as reflecting differences in the availability of unweathered bedrock across the Efri Haukadalsá catchment, with V-shaped valleys having greater access to fresh sulfide-bearing minerals than alluviated U-shaped valleys; this interpretation is in contrast to one in which the elevated $\delta^{34}S_{SO4}$ values reflect fractionation during sulfur transformations along alluvial reaches. These results validated the application of river inversion models for constraining weathering fluxes and affirmed that pyrite oxidation globally, even in the presence of river sulfur cycling, modulates the abundance of atmospheric carbon dioxide.

1. Introduction

Chemical weathering regulates the concentration of atmospheric carbon dioxide (CO_2) by sourcing alkalinity and dissolved inorganic carbon into the coupled ocean-atmosphere system (Walker et al., 1981). While weathering of silicate minerals was previously thought to largely control atmospheric CO_2 over geologic timescale, studies have now also demonstrated that ubiquitous oxidation of pyrite (FeS_2) to sulfuric acid removes alkalinity from the ocean-atmosphere system and partially compensates for CO_2 drawdown associated with silicate weathering (Calmels et al., 2007; Torres et al., 2014, 2016; Burke et al., 2018; Kemeny et al., 2020). Quantifying the climatic and lithologic controls of FeS_2 oxidation during weathering have thus emerged as important questions in study of the global carbon, sulfur, and alkalinity cycles.

* Corresponding author.
E-mail addresses: pkemeny@caltech.edu, preston.kemeny@gmail.com (P.C. Kemeny).

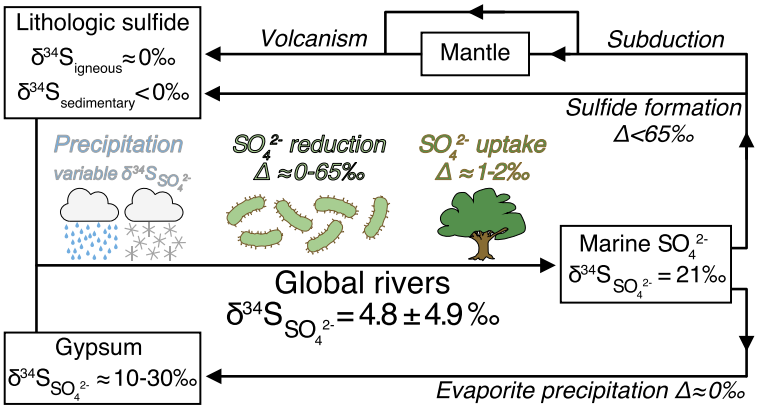

Fig. 1. Schematic of the global sulfur cycle. River $[SO_4^{2-}]$ and $\delta^{34}S_{SO4}$ have been used to quantify chemical weathering reactions and the associated biogeochemical fluxes of alkalinity and dissolved inorganic carbon in rivers globally. Additionally, river $[SO_4^{2-}]$ and $\delta^{34}S_{SO4}$ have been used to constrain the abundance and $^{34}S/^{32}S$ ratio of SO_4^{2-} input to seawater, which are key parameters in biogeochemical models interpreting geologic records of $\delta^{34}S$ and $\delta^{13}C$ (Kump and Garrels, 1986). However, rivers may host fractionating processes such as dissimilatory microbial SO_4^{2-} reduction or SO_4^{2-} assimilation that could bias the results of river inversion calculations and biogeochemical models. The given range of river $\delta^{34}S_{SO4}$ values is from Burke et al. (2018), gypsum $\delta^{34}S$ was assumed to span the $^{34}S/^{32}S$ range of Phanerozoic evaporites, the $\delta^{34}S$ of igneous sulfide was assumed to match bulk terrestrial sulfur, and the range of fractionations associated with MSR was estimated from laboratory culture studies.

Quantifying the role of FeS_2 oxidation during weathering requires apportioning measurements of river sulfate (SO_4^{2-}) between multiple sources such as meteoric precipitation, evaporite dissolution, and hydrothermal fluids (Gaillardet et al., 1999; Burke et al., 2018). This attribution often relies on inversion models that assume dissolved river chemistry reflects conservative mixing of a limited number of end-members with constrained elemental and isotopic compositions. However, researchers have suggested that microbial sulfate reduction (MSR) and SO_4^{2-} assimilation may alter the abundance and/or $^{34}S/^{32}S$ isotope ratio of fluvial SO_4^{2-} ($\delta^{34}S_{SO4}$) during transport (Fig. 1). Evidence of MSR impacting $\delta^{34}S_{SO4}$ comes from the Marsyandi River in the Nepal Himalaya, where researchers found coherent relationships among the concentration of sulfate ($[SO_4^{2-}]$), the value of $\delta^{34}S_{SO4}$, and the major and minor oxygen isotope ratios of SO_4^{2-} (Turchyn et al., 2013; Hemingway et al., 2020). More broadly, sulfur is an important nutrient for the terrestrial biosphere (Kertesz and Mirleau, 2004) and sulfur cycling associated with plant uptake and growth or the recycling of plant-derived biomass within soils and the rhizosphere might engender small but meaningful isotopic fractionations (Trust and Fry, 1992; Tcherkez and Tea, 2013). If biological transformations lead to substantial changes in $\delta^{34}S_{SO4}$ then $^{34}S/^{32}S$ isotope ratios may not faithfully record weathering processes, affecting estimates of FeS_2 oxidation.

Microbial sulfate reduction is expected to increase residual river $\delta^{34}S_{SO4}$ to values above the primary lithologic sources of sulfur. Were such a process widespread, this increase would force river inversion models to calculate larger contributions from high-$\delta^{34}S$ end-members such as evaporites and meteoric precipitation, with the effect of underestimating the importance of terrestrial FeS_2 oxidation. Moreover, measurements of river $\delta^{34}S_{SO4}$ form an important boundary condition for global isotope mass balance models involving the sulfur cycle and its connections to carbon cycling and atmospheric dioxygen (Kump and Garrels, 1986). If values of river $\delta^{34}S_{SO4}$ are elevated due to microbial activity these models may be systematically biased towards reconstructing lower fractions of FeS_2 burial across geologic time.

Evaluating the importance of in-catchment sulfur cycling requires quantifying the relative export and storage of organic and inorganic sulfur. Export of inorganic sulfur as species other than SO_4^{2-}, such as detrital minerals or gaseous H_2S, is unexpected in oxygenated surface environments based on both theoretical calculations of mineral oxidation kinetics (Johnson et al., 2014) and direct observations of atmospheric gases (Andreae et al., 1990). The greater stability of organosulfur species (Xia et al., 1998) suggests that particulate and dissolved organic phases may provide a reduced sulfur flux, yet direct observations are currently lacking. Identifying sulfur transformations from existing dissolved data is complicated by the presence of multiple weathering lithologies in most catchments, each of which may carry a variable range of $\delta^{34}S$ values (Calmels et al., 2007; Kemeny et al., 2020).

In this work we studied weathering, sediment transport, and sulfur cycling in river catchments of western Iceland. Due to the catchments' relatively uniform basaltic bedrock lithology, fluvial sulfur transformations were expected to be easier to diagnose than in catchments containing diverse lithologies. Our approach was further bolstered by previous work on the $^{34}S/^{32}S$ isotope ratio of Icelandic rocks (Sakai et al., 1980; Torssander, 1989; Hildebrand and Torssander, 1998; Stefánsson et al., 2015) and prior measurements of $\delta^{34}S_{SO4}$ in Icelandic rivers (Gislason and Torssander, 2006; Robinson et al., 2009).

2. Methods

2.1. Field sites

River water and sediment samples were collected from the Efri Haukadalsá river catchment and surrounding region during two field campaigns in August 2016 and July-August 2019 (Fig. 2; Appendix A, Figs. A.1, A.2, and A.3 for drone imagery and field photographs). Carbon analyses from the 2016 field season, including ^{14}C dates, $\delta^{13}C$ measurements, and estimates of the amount of alluvial fill in the catchment, were previously reported in Torres et al. (2020).

The Efri Haukadalsá is a meandering river constructing a prograding delta as it drains into lake Haukadalsvatn (Fig. 2C). A sediment core from Haukadalsvatn containing glacial dropstones and marine mollusk shells below finely laminated lacustrine sediment indicated that the catchment deglaciated ~13 ka and was only briefly marine before reflecting the deposits from the active fluvial-deltaic-lacustrine source-to-sink system (Geirsdóttir et al., 2009). The 170 km^2 Efri Haukadalsá catchment does not currently contain glaciers. The catchment lies within late Miocene (5.3–11 Ma) basaltic and intermediate extrusive rocks, although a small exposure of silicic rock is reported in the headwaters of tributary 3 (Hjartarson and Sæmundsson, 2014) (Fig. 2). The Efri Haukadalsá catchment is far from Iceland's primary hydrothermal axis and current volcanic or hydrothermal inputs are expected to be negligible;

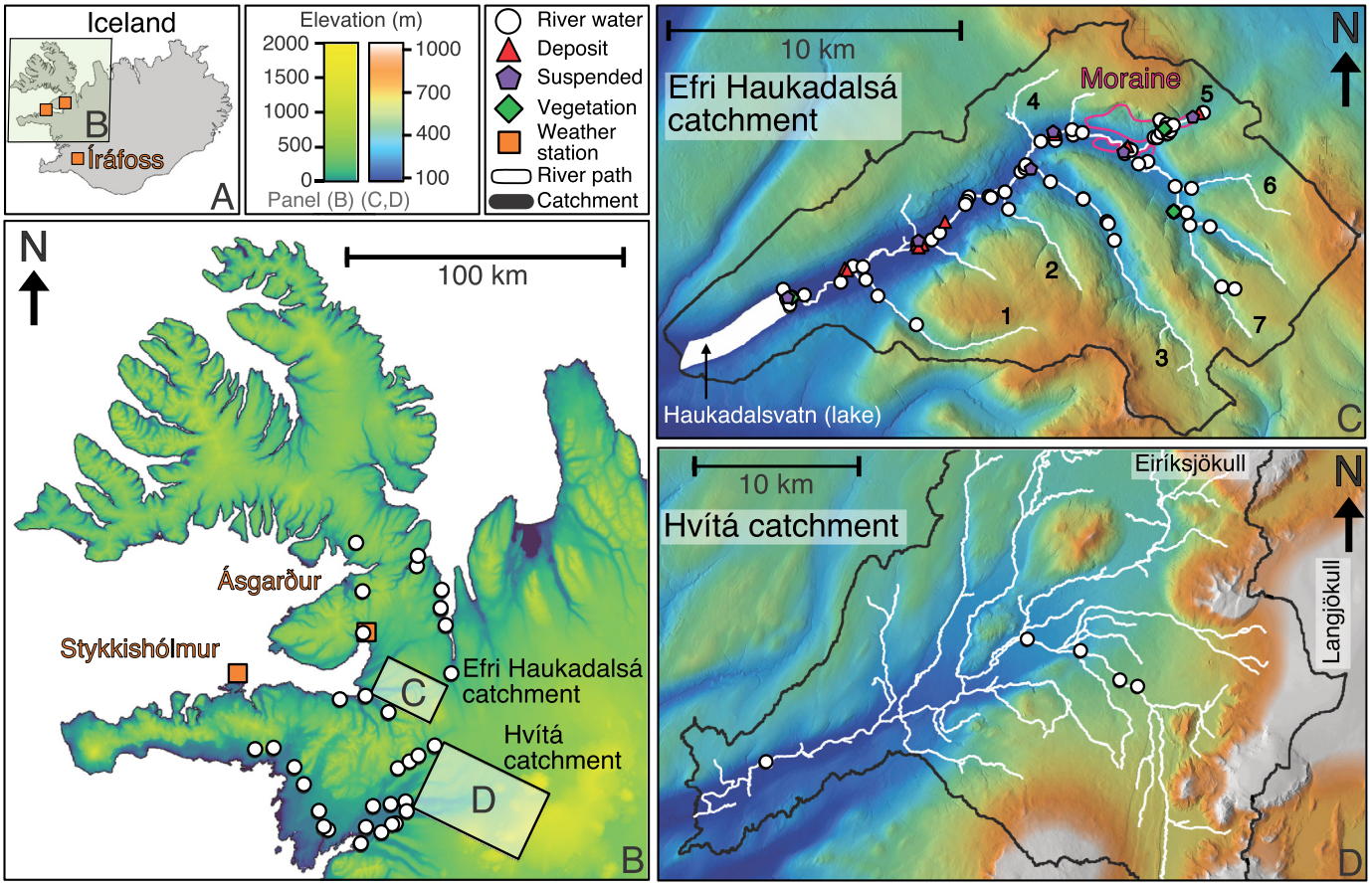

Fig. 2. Sampling sites. (A) Iceland with indicated study region and relevant meteorological stations (orange squares). Coastline data were sourced from the European Environment Agency in EPSG 3035. (B) Western Iceland with river water sampling locations (white circles). Boxed regions show the Efri Haukadalsá catchment and the Hvítá catchment. Elevation data were sourced from the Icelandic Land Survey in EPSG 3057. (C) The Efri Haukadalsá catchment with indicated sampling locations for river water samples (white circles), deposit samples (red triangles), suspended sediment samples (purple pentagons), and vegetation samples (green diamonds, locations approximate). The location of a moraine is indicated. Tributaries are numbered following Torres et al. (2020). (D) The Hvítá catchment with indicated sampling locations. Elevation data for the Efri Haukadalsá and Hvítá catchments were sourced from the Polar Geospatial Center in EPSG 3413. Note that the north arrow rotates between panels due to change of projection. (For interpretation of the colors in the figure(s), the reader is referred to the web version of this article.)

no visual indicators of hydrothermal activity were observed. The presence of calcite and zeolites in vugs suggests that some basalt beds may have previously been hydrothermally altered, although such features could also have formed through groundwater influences. Porosity is largely sealed in this region due to secondary mineralization, causing surface runoff to dominate over groundwater flow (Gislason et al., 1996). Vegetation in the catchment is currently dominated by grasses and sedges, but site names indicate that the region was previously forested (Geirsdóttir et al., 2009).

The Efri Haukadalsá is alluvial for much of its length, but with bedrock exposures in some tributaries, and is mostly gravel-bedded, but with a transition to sand-bedding near Haukadalsvatn (Torres et al., 2020). The lower section of the mainstem Efri Haukadalsá has a U-shaped cross section and the channel is alluvial in this lower valley, meandering across a floodplain approximately 600–800 m wide (Fig. 2C). This channel and floodplain material are part of a relatively thick alluvial fill that is likely the result of fluvial and lacustrine deposition following deglaciation (Geirsdóttir et al., 2009; Torres et al., 2020). Several steep tributaries branch from the lower section of the Efri Haukadalsá mainstem. Tributaries 1 and 2 enter the mainstem near Lake Haukadalsvatn and upstream of the lower reach, respectively (Figs. 2C, A.1). A major split in the Efri Haukadalsá occurs about halfway upstream, after which both branches curve in parallel toward the southeast. The lower branch of the split, tributary 3, is a hanging valley off the mainstem, separated by a steep knickzone. On the basis of dissolved chemistry, we calculated that tributary 3 supplied 26 ± 7% (2σ) of the water flow downstream of the confluence. Tributaries 1, 2, and 3 tended to have only a thin cover of sediment, typical of bedrock rivers, and lacked the thick alluvial fill of the lower mainstem valley. In the upper branch of the split, there is a moraine along tributary 5 (Fig. 2C, pink outline). Two bedrock knickpoints occur in the Efri Haukadalsá mainstem, the first near the confluence with tributary 3 and the second near the site of sediment input from the moraine. Emergent springs with conspicuous iron oxide deposits were identified throughout the catchment, which we refer to as “Fe springs” (Fig. A.2F). River water samples were classified on the basis of either location (mainstem, tributary, lake), notable geomorphologic features (draining the moraine), or visual indicators of chemistry (Fe springs).

Thirty-two additional water samples from outside of the Efri Haukadalsá catchment were collected during the 2016 field campaign (Fig. 2B) which we refer to as “NW rivers”, and seven additional water samples from five sites along the Hvítá river and its tributaries were sampled from a catchment draining the Langjökull and Eiríksjökull glaciers during the 2019 field season (Fig. 2D). The former sampling sites were more coastal than the Efri Haukadalsá and included catchments with increased exposures of felsic lithologies (Gislason et al., 1996; Hjartarson and Sæmundsson, 2014); this shift in underlying lithology is expected to impact dissolved ion concentrations but have little impact on $\delta^{34}S_{SO4}$ (Torssander,

1989). The catchment of the Hvítá river includes mafic and intermediate lithologies (Gislason et al., 1996).

2.2. Sample collection

In August of 2016, water samples were collected directly from the rivers in single-use syringes and passed through 0.2 µm nylon porosity filters into two 15 ml sampling tubes. Syringes were rinsed with river water and containers with eluate prior to collection, and one split was acidified with concentrated high-purity HNO_3 dispensed from a FEP dropper bottle. Precipitation was collected into a bowl approximately 35 km south of Haukadalsvatn during six rain events; this sampling site was further inland than the Efri Haukadalsá catchment and located about 200 m from Route 1. Precipitation samples were processed in the same fashion as the river samples. Two rain events were sampled twice, with one of each sampling lacking an acidified split.

In August 2019, most river water samples were filtered through a 0.22 µm porosity nylon syringe filter into two eluate-rinsed 50 ml sampling tubes, one of which was acidified with high-purity HNO_3. Several river samples were collected in duplicate using a motorized peristaltic pump, a polypropylene 142 mm filter holder, and 0.2 µm porosity nitrocellulose mixed ester filter; no chemical differences were discernible between the methods. In 2019, a single rain sample was collected from the field site using an HDPE funnel atop an upright HDPE container, and was not acidified due to low collected volume. Two samples of seasonal snow were collected from tributary 7 in the catchment headwaters of the Efri Haukadalsá (Fig. 2C), as well as one sample of ice from Langjökull glacier. We did not determine $[SO_4^{2-}]$ for these snow and ice samples due to analytical detection limits and did not measure $\delta^{34}S_{SO4}$. For comparison, prior measurements of $\delta^{34}S$ and Cl^-/SO_4^{2-} in ice from Langjökull glacier were digitized from Fig. 7 of Gislason and Torssander (2006).

Suspended sediment, deposited sediment, and vegetation samples were also collected from the Efri Haukadalsá catchment. Suspended sediment was sampled in 2016 through large-volume (~30–80 L) filtrations using 0.3 µm pre-combusted Glass Fiber Filters and was given the sample prefix "LHWS" (Fig. 2C, purple pentagons). Floodplain deposits were logged and sampled with hand auger or by river cut-bank exposures, with multiple depths sampled from within each stratigraphic section (Fig. 2C, red triangles). Deposit sites were given the sample prefix "LHSS" and were lyophilized and homogenized prior to isotopic or synchrotron analysis (Torres et al., 2020). All filter samples were stored frozen, and lyophilized and homogenized sediment samples were stored at room temperature. Additionally, five vegetation samples, given the sample prefix "LHVS", were collected from the Efri Haukadalsá catchment in 2019 (Fig. 2C, green diamonds). After being lyophilized, a subset of each vegetation sample was ground in liquid nitrogen using a pre-combusted mortar and pestle cleaned between samples with quartz abrasive and organic solvent.

2.3. Ion chromatography

The dissolved concentrations of major cations and anions were quantified in the Environmental Analysis Center at the California Institute of Technology. A Dionex ICS-2000 with CG12A guard column (2 mm × 50 mm), CS12A separator column (2 mm × 250 mm), and 20 mM isocratic methanesulfonic eluent was used to quantify $[Ca^{2+}]$, $[Mg^{2+}]$, $[Na^+]$, and $[K^+]$. A Dionex ISC-3000 with AG29 guard column (2 mm × 50 mm), AS29 separator column (2 mm × 250 mm), and 4.5 mM/2.5 mM Na_2CO_3 / $NaHCO_3$ isocratic eluent was used to quantify $[SO_4^{2-}]$ and $[Cl^-]$. All chromatography measurements were made with suppressed conductivity detection. Precision was quantified through repeated measurements of MAURI-09 and CRANBERRY-05 from Environment and Climate Change Canada. The relative standard deviation was better than 4.1% (1σ) for all elements other than Ca^{2+}, which was 6.7% (1σ) for MAURI-09. No SO_4^{2-} data were available for three snow/ice samples due to detection limits, and no cation data were available for the two rain samples lacking acidified splits (Appendix B, Fig. B.1). The concentration of HCO_3^- was calculated by charge balance.

2.4. MC-ICP-MS measurements of $\delta^{34}S_{SO4}$

River water and precipitation $\delta^{34}S_{SO4}$ values were measured by Multicollector Inductively Coupled Plasma Mass Spectrometry (MC-ICP-MS) at the California Institute of Technology following an adapted method of Paris et al. (2013). Briefly, SO_4^{2-} was isolated using AG 1-X8 analytical grade 100-200 mesh chloride form anion-exchange resin, matrix matched to an in-house Na_2SO_4 standard, and measured with sample-standard bracketing. Outlier $^{34}S/^{32}S$ determinations were identified statistically ($>3\sigma$) and visually when associated with substantial loss of signal intensity and removed from the analysis, as were entire sets of measurement cycles following large changes in mass biasing. The average blank of column chromatography was 0.4 nmol SO_4^{2-}, and we report $\delta^{34}S_{SO4}$ values calculated from the mean of blank-corrected $^{34}S/^{32}S$ ratios. Consistency standards included seawater ($\delta^{34}S_{SO4} = 20.9 \pm 0.5‰$; 2σ, n = 50 aggregating measurements of natural seawater and IAPSO seawater) and the in-house reference material Switzer Falls ($\delta^{34}S_{SO4} = 4.2 \pm 0.4‰$; 2σ, n = 56) (Burke et al., 2018). The standard deviation of the distribution of error-normalized deviations ranged from 2.0 to 9.5 across 11 analytical sessions (John and Adkins, 2010). The $^{34}S/^{32}S$ ratio was measured at least twice on all 121 river water and precipitation samples. Furthermore, 44 samples were processed through column chromatography at least twice; for the 38 of these samples measured only twice, the mean of two times the absolute difference in $\delta^{34}S_{SO4}$ between the two determinations was 0.5‰. We report error as the larger of either the reproducibility of consistency standards or the standard deviation of replicate blank-corrected $^{34}S/^{32}S$ determinations.

2.5. EA-IRMS measurements of deposit $\delta^{34}S$

The $\delta^{34}S$ value of 20 deposit samples was measured using a Thermo Flash Elemental Analyzer coupled through a Conflo-IV interface to a Thermo Delta V isotope ratio mass spectrometer. Most samples were burned in the presence of V_2O_5 and $^{34}S/^{32}S$ ratios were corrected for the capsule blank. Measurements were calibrated to the VCDT scale using IAEA-S1 and IAEA-S2. For samples measured once (7/20), we assigned error as the precision of replicate $\delta^{34}S$ determinations on sample LHSS-07, 137 cm (2σ = 0.8‰, n = 10), which is the sample with the most measurements. For samples measured multiple times (13/20), we assigned error as the larger of either the standard deviation of replicate $\delta^{34}S$ values or the reproducibility of sample LHSS-07, 137 cm. We compared sediment $\delta^{34}S$ values with previously published observations (Torres et al., 2020) of $\delta^{13}C$ and fraction modern ($(^{14}C/^{12}C)_{sample}/(^{14}C/^{12}C)_{standard}$, corrected for mass-dependent stable isotope fractionation using measured $^{13}C/^{12}C$).

2.6. X-ray absorption near edge structure spectroscopy

X-ray Absorption Near Edge Structure (XANES) spectroscopy measurements across the sulfur K-edge using an X-ray microprobe provided micron-scale information on the electronic structure and redox state of sulfur in our solid phase samples. XANES measurements were conducted on suspended sediment, deposit samples,

and vegetation samples at beamline 14-3 of the Stanford Synchrotron Radiation Lightsource at the SLAC National Accelerator Laboratory. The X-ray microprobe beam was focused to ~5 μm using K-B mirrors and calibrated to define the first pre-edge feature of sodium thiosulfate at 2472.02 eV. Subsamples of filters with suspended sediment were directly attached to sampling trays, while deposit samples and vegetation samples were typically prepared by inverting homogenized powders onto tape. Most samples were initially mapped at or above the sulfur K-edge at 20-25 μm resolution to identify sulfur-rich regions, which were then mapped at 5 μm resolution and multiple energies characteristic of the resonances of specific sulfur species. Principle Component Analysis within the high-resolution map region identified points of interest for sampling chemical diversity, which were selected for collection of complete X-ray absorption spectra. Because this method characterized the spectral diversity of a sample, the data should not be viewed as a random survey. During the measurements we identified an oxidized sulfur blank on the filters used to sample suspended sediment, but testing revealed that the blank was highly soluble and was likely removed during sample collection (Appendix C, Torres et al., 2020).

Replicate X-ray absorption spectra were averaged and baseline corrected using the SIXPACK software package (Webb, 2005). Several averaged spectra (18/184) displayed high noise relative to the maximum fluorescence, interpreted as low sulfur abundance, and were excluded from subsequent analysis. Remaining spectra (166/184) were fit between 2470 eV and 2490 eV to spectra of standard materials containing thiol, disulfide, sulfoxide, sulfonate, and sulfate from the ID 21 database of the European Synchrotron Radiation Facility (Bohic et al., 2008). Fitting was done in MATLAB as an optimization to minimize proportional misfit, where fractional contributions were constrained to be positive but with an unconstrained sum, and the optimization utilized a normalized fluorescence threshold of 0.1 (Prietzel et al., 2011; Manceau and Nagy, 2012). We quantified speciation as the fit of each reference spectra normalized to the sum of all contributions, and defined a statistic, $F_{reduced}$, as the sum of fractional contributions from the thiol, disulfide, and sulfoxide moieties. This statistic integrated the relative abundance of organic sulfur (S_{org}) species that are particularly reactive in the presence of dioxygen and other high-potential redox species in the environment (e.g. manganese oxides).

After aggregating data in the software package SMAK (Webb, 2011), maps of $F_{reduced}$ values were generated in MATLAB through pixel-by-pixel fitting of multiple-energy maps to the same ID 21 standards. The fitting was conducted on pixels with more than 5 counts at an incident energy at or above the sulfur K-edge, and responses of 0 counts for any incident energy were removed prior to fitting. This pixel-by-pixel fitting was validated through comparison with $F_{reduced}$ values derived from complete spectra. By characterizing the sulfur speciation at each pixel of regions mapped with multiple incident energies, we generated a single $F_{reduced}$ value representative of each mapped region. However, because suspended sediment samples were not homogenized prior to synchrotron analysis, mapped regions for these samples were not necessarily representative of the bulk sample.

2.7. Geomorphic analyses

We used Digital Elevation Models (DEM) to quantify the topographic form of the Efri Haukadalsá catchment in order to evaluate relationships between landscape morphology and river $\delta^{34}S_{SO4}$. DEMs were acquired from the Icelandic Land Survey (10m resolution, EPSG 3057 referenced to the GRS 1980 ellipsoid) and Polar Geospatial Center (Arctic DEM Mosaic, 2m resolution, EPSG 3413 referenced to WGS84 ellipsoid). Using TopoToolbox in MATLAB (Schwanghart and Kuhn, 2010) we used the Arctic DEM to generate 405 cross sections at approximately constant spacing throughout the Efri Haukadalsá catchment and conducted three different analyses. The first and second analyses were based on quantitative fitting of models to represent the shape of each valley cross section. In the first analysis, we fit each cross section topography by constraining the variable r, which determined the valley shape from U-shaped to V-shaped, and the variable a, which aligned the valley center, to minimize the function $f(r, a) = (|x - a|^r - y)^2$, where x represented horizontal distance and y represented elevation (Allen et al., 2018). We performed this fitting both for raw elevation data and after trimming each cross section so that the two sides reached approximately the same elevation, and in both cases the elevation data were normalized to range from 0 to 1 prior to fitting. We reported the mean and range of the shape parameter, r, for the two data reductions. In the second analysis, we identified a central point in each cross section and isolated the continuous section on either side of this point that was neither flat nor decreasing in elevation. We then independently fit each side of the valley to a power law by constraining the variables a, b, and c to minimize the function $f(a, b, c) = (ax^b + c - y)^2$, and reported the mean of the two b values (Appendix F, Fig. F.1). In the third analysis each cross section was, in a random order, visually inspected and manually assigned to one of five categories: U-shaped with flat bottom, U-shaped with rounded bottom, V-shaped, V-in-U, and N/A. This classification was done in triplicate and the three sets of classifications were mutually consistent. We compared $\delta^{34}S_{SO4}$ and $[SO_4^{2-}]$ to the mean power law exponents r and b and the fraction of V-shaped cross sections upstream of each sampling site. All three geomorphic analyses yielded similar relationships.

3. Results

Ternary diagrams of cation and anion concentrations characterized the dissolved chemistry of samples (Fig. 3). The ion Ca^{2+} comprised between 23% and 60% of the cation charge in river waters, Na^+ sourced 19% to 68%, Mg^{2+} was 7% to 36%, and K^+ made up only 1% to 2%, as charge equivalent ratios (Fig. 3A). Samples from NW Iceland, which tended to be from locations closer to the coast than samples from the Efri Haukadalsá, were enriched in $(Na^+ + K^+)/\Sigma^+$ relative to samples from the Efri Haukadalsá ($\Sigma^+ = 2^*Ca^{2+} + 2^*Mg^{2+} + Na^+ + K^+$). Within the Efri Haukadalsá, a subset of tributaries and samples near the moraine and Fe springs were relatively depleted in $(Na^+ + K^+)/\Sigma^+$ and enriched in Ca^+/Σ^+. Overall, samples had lower values of Mg^{2+}/Σ^+ than expected from conservative mixing between basalt weathering and annually-integrated precipitation, consistent with prior observations (Gislason et al., 1996). Summertime precipitation samples and ice samples formed an array between high Ca^+/Σ^+ and high $(Na^+ + K^+)/\Sigma^+$ with low Mg^{2+}/Σ^+.

The anions HCO_3^- and Cl^- dominated the anion budget of river water samples (Fig. 3B). The ion Cl^- accounted for 10% to 44% of anion charge, with higher fractions in samples from NW Iceland, and HCO_3^- constituted between 49% and 87% of charge. Except in a single sample from outside of the Efri Haukadalsá catchment, SO_4^{2-}/Σ^+ was between 1% and 12% in all river samples. The anion SO_4^{2-} comprised a larger fraction of the charge budget in precipitation than in river water.

Values of $\delta^{34}S_{SO4}$ ranged from 0.6‰ to 23.7‰ in all river water samples and ranged from 2.5‰ to 23.7‰ in samples from the Efri Haukadalsá (Fig. 4). Measured $\delta^{34}S_{SO4}$ in precipitation ranged from 6.2‰ to 18.1‰ (Fig. 4A). In samples from the Efri Haukadalsá, $\delta^{34}S_{SO4}$ values increased with $1/SO_4^{2-}$ (Fig. 4B). Moreover, measurements of $\delta^{34}S_{SO4}$ values fell along linear arrays when plotted

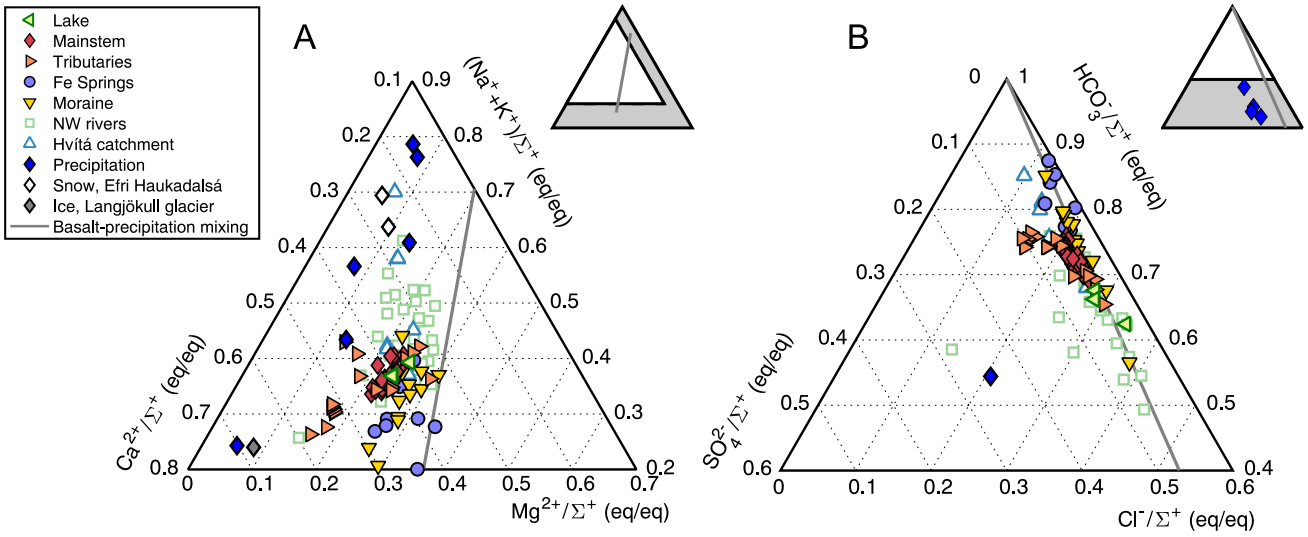

Fig. 3. Cation and anion ternary diagrams. Plotted data are ratios of charge-equivalent concentrations uncorrected for Cl^- inputs from precipitation, and the plotted regions are subsets of the full parameter space (as indicated in the schematic to the top-right above each panel: filled white triangles are plotted areas and the grey triangles indicate the full space). (A) Cation ternary diagram of Ca^{2+}–Mg^{2+}–Na^++K^+ for all samples. River waters from the Efri Haukadalsá tended to have higher Ca^{2+}/Σ^+ and lower $(Na^+ + K^+)/\Sigma^+$ than samples from NW Iceland or from the Hvítá catchment. All river water samples plotted away from a mixing line between basalt and annually-integrated precipitation (grey line), indicating depletion in Mg^{2+}/Σ^+ relative to two-component mixing. As previously suggested (Gislason et al., 1996) and supported by inversion modeling with Monte Carlo error propagation (Appendix E, Figs. E.1, E.2), we attributed this depletion to the formation of secondary clays. Three precipitation samples lacking measurements of Σ^+ were not plotted. (B) Anion ternary diagram of SO_4^{2-}–Cl^-–HCO_3^- for all samples. The anion HCO_3^-, quantified through charge balance, was the dominant anion in solution. The ion Cl^- was the second most abundant anion and samples from NW Iceland were enriched in Cl^-/Σ^+ relative to samples from the Efri Haukadalsá, consistent with their elevated values of $(Na^+ + K^+)/\Sigma^+$. Most samples had $SO_4^{2-}/\Sigma^+ < 12\%$ (eq/eq). The anion SO_4^{2-} comprised a larger fraction of charge in precipitation samples (blue diamonds in top-right schematic). One precipitation sample with $(Cl^- + SO_4^{2-})/\Sigma^+ > 1$ was not plotted. The anion data were largely consistent with mixing between basalt and annually-integrated precipitation.

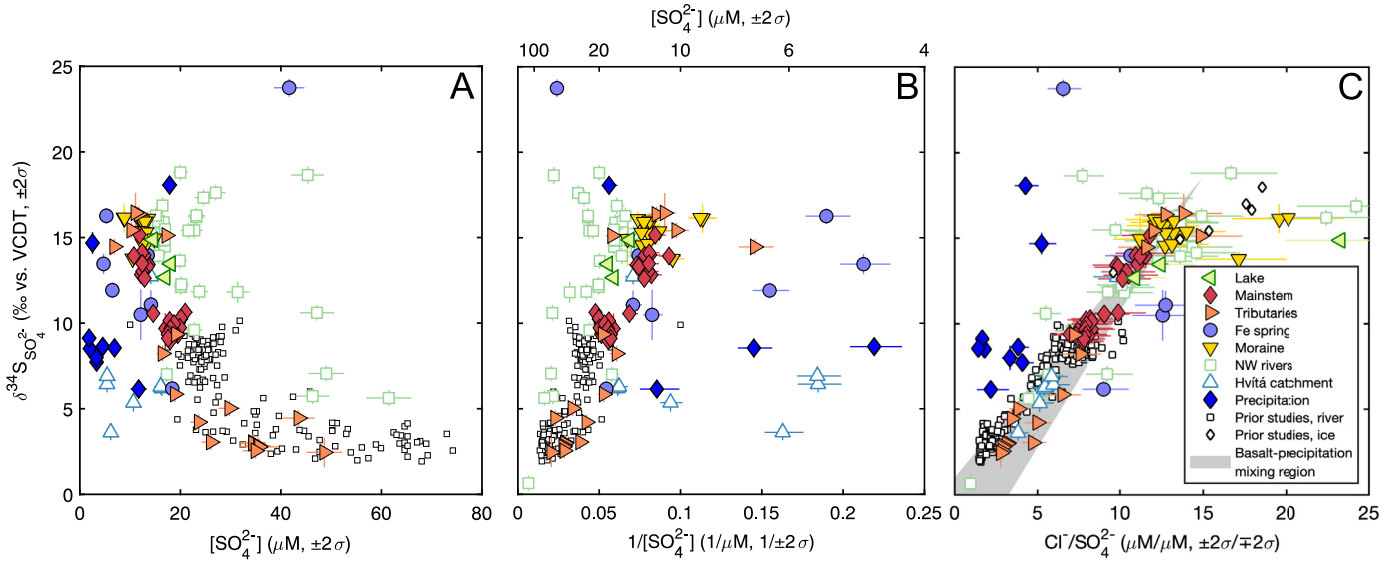

Fig. 4. $\delta^{34}S_{SO4}$, $[SO_4^{2-}]$, and Cl^-/SO_4^{2-} of river water samples. (A) $\delta^{34}S_{SO4}$ decreased with increasing $[SO_4^{2-}]$. (B) $\delta^{34}S_{SO4}$ was linear with $1/SO_4^{2-}$, excluding samples from Fe springs. (C) $\delta^{34}S_{SO4}$ against Cl^-/SO_4^{2-}. The data were well described by mixing between a low-$\delta^{34}S$ end-member and a high-$\delta^{34}S$ end-member, proposed to be basalt and precipitation, respectively. Note that the end-members of the mixing line (grey) were independently constrained and not fit through our river water measurements. The plotted basalt end-member had $\delta^{34}S$ ranging from −2‰ to 1‰ and Cl^-/SO_4^{2-} between 0 and 2 (Sakai et al., 1980; Torssander, 1989). The precipitation end-member had $\delta^{34}S_{SO4}$ derived from our observations and the precipitation intensity recorded at the Ásgarður and Stykkishólm meteorological stations, and Cl^-/SO_4^{2-} based on the observed chemistry of precipitation at the Íráfoss meteorological station (Appendix D). Several precipitation samples are out of the plotting range in (B) and three Fe springs samples with elevated Cl^-/SO_4^{2-} ratios are out of range in (C). Prior observations of river $\delta^{34}S_{SO4}$ and Langjökull $\delta^{34}S$ are from Gislason and Torssander (2006).

against Cl^-/SO_4^{2-} (Fig. 4C). Repeat sampling of the Efri Haukadalsá indicated that river $\delta^{34}S_{SO4}$ was largely constant in time (Appendix H, Table H.1); conversely, we identified slight temporal changes in the dissolved chemistry of Haukadalsvatn (Appendix I).

The sulfur content of floodplain deposits ranged from 0.025 wt.% to 1.01 wt.% and sediment $\delta^{34}S$ values ranged from 11.1‰ to 17.8‰ (Fig. 5). With the exception of the organic carbon-rich site LHSS-07 and the site LHSS-04, sediment $\delta^{34}S$ values were relatively constant at a single location while sulfur contents were variable across samples (Fig. 5A, 5B). At LHSS-07, sulfur contents were relatively uniform across samples while $\delta^{34}S$ values ranged from 12.6‰ to 17.8‰. Sediment $\delta^{34}S$ values were poorly corre-

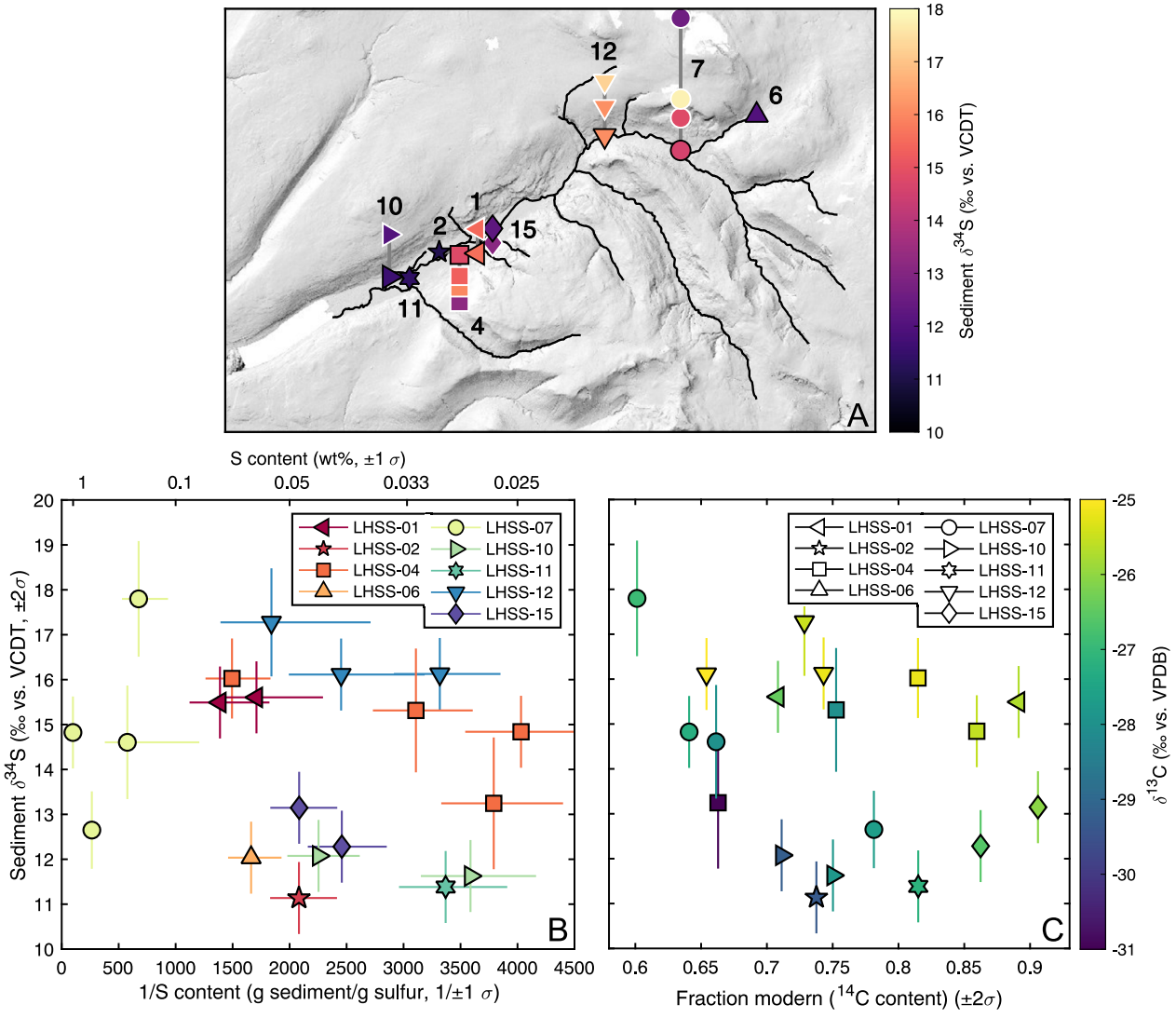

Fig. 5. Sediment δ^{34}S. (A) $^{34}S/^{32}S$ isotope ratio by sampling location. Numbers refer to sediment sampling sites, which are coded by plotting symbol, and multiple points per symbol reflect vertical sampling. Markers with black edges indicate the ground surface or river surface; markers with white edges below these indicate depth below surface, while markers with white edges above these indicate height above the river. Points that would otherwise overlap are partially offset from one another; true sampling locations are plotted in Fig. 2C. (B) Sediment $^{34}S/^{32}S$ ratio against inverse sulfur content. Except for LHSS-07 and LHSS-04, samples from the same site generally had similar δ^{34}S values but variable sulfur abundances. At LHSS-07, all samples had high sulfur abundances but variable $^{34}S/^{32}S$ ratios. (C) Sediment δ^{34}S against fraction modern (^{14}C content) color-coded by δ^{13}C. There was no clear relationship between sediment δ^{34}S value and ^{14}C content. The fraction modern of the sample from the moraine (LHSS-06) had a value of 0.27 and is not plotted.

lated with ^{14}C abundance and only weakly related to δ^{13}C values (Fig. 5C).

X-ray absorption spectra revealed a range of organic sulfur moities in suspended sediment, deposit samples, and vegetation (Fig. 6A). Flourscence peaks corresponding to organic disulfide (e.g. oxidized glutathione), thiol, sulfoxide, sulfonate, and sulfate moities were observed across vegetation, suspended sediment, and deposit samples (Fig. 6B).

4. Discussion

4.1. Source of ions to river water

The linear trend defined by $\delta^{34}S_{SO4}$ and Cl^-/SO_4^{2-} (Fig. 4C) was consistent with two end-member mixing, where SO_4^{2-} in the Efri Haukadalsá was predominantly sourced from a low-δ^{34}S, low Cl^-/SO_4^{2-} end-member and a high-δ^{34}S, high Cl^-/SO_4^{2-} end-member. We proposed that the low-$^{34}S/^{32}S$ end-member was basalt and the high-$^{34}S/^{32}S$ end-member was annually-integrated precipitation, where the latter reflected the sum of distinct summertime and wintertime meteoric inputs (Appendix D; Torssander, 1989; Gislason et al., 1996; Moulton et al., 2000; Gislason and Torssander, 2006; Bern et al., 2015).

The δ^{34}S value of Icelandic basalt ranges from approximately −2‰ to 2.5‰ with a mean value of −0.5±2.4‰ (2σ) (Sakai et al., 1980; Torssander, 1989; Hildebrand and Torssander, 1998). The δ^{34}S of rhyolite is 1–2‰ higher than basalt and with lower sulfur abundance (Torssander, 1989). The sulfur content of Icelandic basalt is approximately 150 ± 160 ppm (1σ) (Sakai et al., 1980; Torssander, 1989) and the chlorine content is approximately 235 ± 140 ppm (1σ) (Sigvaldason and Óskarsson, 1976), giving an expected Cl^-/SO_4^{2-} molar ratio of approximately 1.4.

We calculated a molar Cl^-/SO_4^{2-} ratio of 14.9 and $\delta^{34}S_{SO4}$ value of 18.5‰ for annually-integrated precipitation based on our samples of summer precipitation, prior observations of precipitation chemistry at the Íráfoss meteorological station, and prior observations of precipitation intensity at the Ásgarður and Stykkishólm meteorological stations (Figs. 2A, 2B; Appendix D, Figs. D.1–D.4).

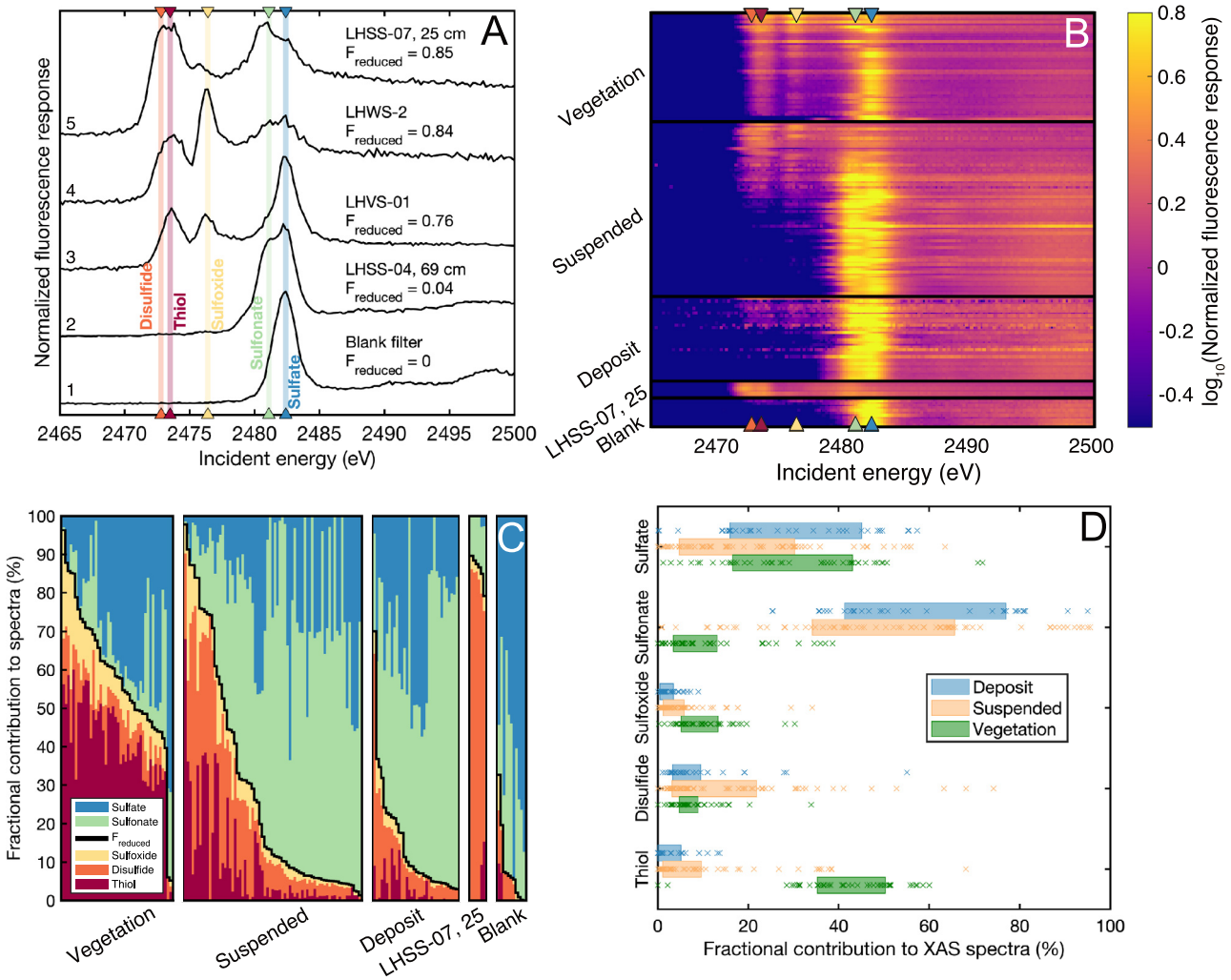

Fig. 6. X-ray spectroscopy results and fitting. XANES identified reduced and oxidized sulfur moieties in suspended sediment, deposit sediment, and vegetation samples. (A) Example X-ray absorption spectra from (1) blank filter, (2, 5) deposit samples, (3) vegetation, and (4) suspended sediment. The statistics $F_{reduced}$ quantified the contribution of thiol, disulfide, and sulfoxide to each spectra relative to the contributions of all moieties. (B) Top-down view of X-ray absorption spectra. Within each category, spectra are organized with higher $F_{reduced}$ values at the top to lower $F_{reduced}$ values at the bottom. The spectra showed peaks at incident energies characteristic of the resonances for reduced sulfur phases such as disulfide, thiol, and sulfoxide. (C) Stacked bar chart showing the fractional contributions of sulfate, sulfonate, sulfoxide, disulfide, and thiol to spectra collected on vegetation, suspended sediment, deposit samples, and blank filters. (D) Fractional contributions arranged by moiety. Thiols made a large contribution to spectra collected on vegetation, while sulfonates made a large contribution to the spectra collected on suspended sediment and deposit samples. Shaded boxes extend from the 25th to 75th percentiles of results.

Approximately 70–80% of this annual precipitation was estimated to fall outside of the summer months with Cl^-/Na^+, Cl^-/Ca^{2+}, Cl^-/Mg^{2+}, and Cl^-/SO_4^{2-} ratios similar to seawater. The remaining fraction of annual precipitation was estimated to fall from May through August with decreased Cl^-/SO_4^{2-} and Cl^-/Ca^{2+} ratios compared to seawater values (Appendix D, Figs. D.1–D.4).

A river mixing model with Monte Carlo error propagation confirmed that dissolved SO_4^{2-} was predominantly sourced from basalt and wintertime precipitation, with a secondary contribution from summertime precipitation (Appendix E, Figs. E.1, E.2). Allowing for formation of a secondary phase with relatively low Na^+/Σ^+ and elevated Ca^{2+}/Σ^+ and Mg^{2+}/Σ^+ ratios recreated our observations of dissolved cation ratios. The results of our inversion model were thus consistent with prior observations of secondary clay formation in Icelandic catchments (Gislason et al., 1996; Thorpe et al., 2019).

4.2. Catchment geometry regulated pyrite oxidation

The fraction of SO_4^{2-} sourced from basalt or from seasonal precipitation in river water samples from the Efri Haukadalsá displayed spatial structure linked to landscape processes (Fig. 7; Appendix G, Fig. G.1). Overall, $[SO_4^{2-}]$ was low (Fig. 7A) and $\delta^{34}S_{SO4}$ values were high (Fig. 7B) in samples from the catchment headwaters and the upper mainstem river, implying that precipitation was the dominant source of SO_4^{2-} to these samples. Conversely, water samples from tributaries 1, 2, and 3 had high values of $[SO_4^{2-}]$ and low values of $\delta^{34}S_{SO4}$, reflecting that basalt weathering was the dominant source of SO_4^{2-} to these samples. Samples from the lower mainstem river had intermediate $[SO_4^{2-}]$ and $\delta^{34}S_{SO4}$ values reflecting a mixture of water derived from the headwaters and from the tributaries.

Values of $[SO_4^{2-}]$ and $\delta^{34}S_{SO4}$ were related to the geometry of valley cross sections upstream of each sampling site (Figs. 7, 8). In the mainstem lower valley, downstream of the confluence with tributary 3, cross sections were U-shaped (Figs. 7D, 7E, 8A, 8F; Appendix F, Fig. F.1), reflecting glacial erosion, with a flat floor defined by postglacial floodplain alluvium. In these reaches the valley bottom has been substantially filled with alluvium, reflecting the progradation and aggradation of the fluvial-deltaic-lacustrine system as it adjusts to the bedrock topography left by glaciation

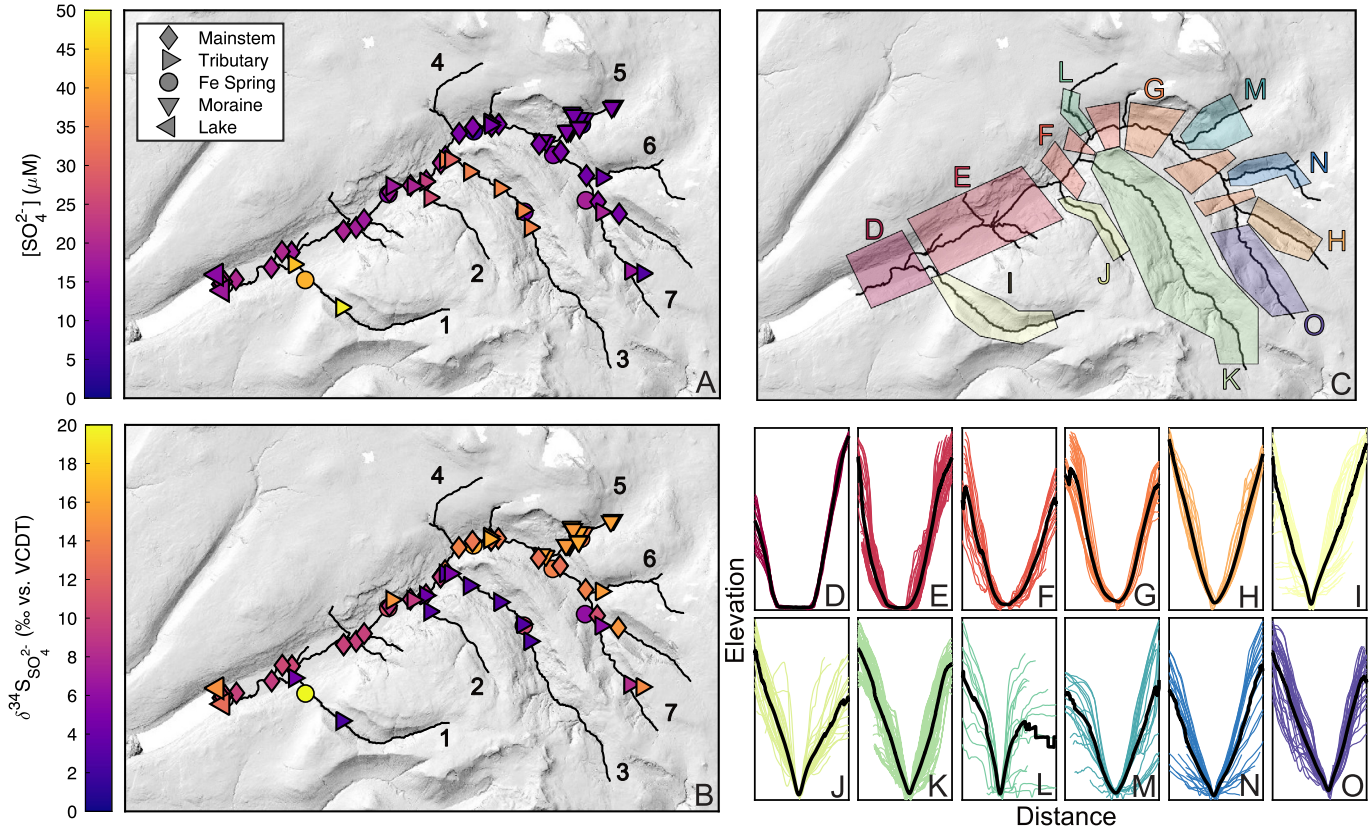

Fig. 7. Spatial structure of $[SO_4^{2-}]$ and $\delta^{34}S_{SO4}$. Maps of (A) $[SO_4^{2-}]$ and (B) $\delta^{34}S_{SO4}$. Values of $[SO_4^{2-}]$ were elevated and $\delta^{34}S_{SO4}$ values were low in samples from tributaries 1, 2 and 3, while values of $[SO_4^{2-}]$ were low and $\delta^{34}S_{SO4}$ values were elevated in samples from the upper section of the mainstem river. In the lower section of the mainstem, SO_4^{2-} and $\delta^{34}S_{SO4}$ had intermediate values. (C) Shaded regions indicate the locations of cross sections show in (D)–(O), where thin colored lines are individual elevation profiles and black lines are averaged cross sections. Averaged cross sections in regions (D)–(H) appeared dominantly U-shaped, consistent with alluviation and higher $\delta^{34}S_{SO4}$ values. Regions (I)–(O) appeared dominantly V-shaped, consistent with fluvial incision and lower $\delta^{34}S_{SO4}$ values. Cross sections in (D)–(O) are presented after both horizontal and vertical alignment.

(Torres et al., 2020). Satellite and drone imagery revealed that the river is meandering through its floodplain deposits in this region, with little connection to bedrock on the steep valley walls (Appendix A, Figs. A.1, A.2, A.3). Above the first knickzone (Fig. 9) the valley cross sections again resembled glacially carved valleys, but with a more parabolic valley floor suggesting less sediment accumulation (Fig. 7F, 7G). We interpreted that SO_4^{2-} in these sites was dominantly sourced from precipitation because bedrock is not exposed on the riverbed, there is likely little fresh FeS_2 in the floodplain deposits, and the floodplain disconnects the river from hillslope bedrock sources. Although the isotopic composition of dissolved SO_4^{2-} in the lower valley was lower than precipitation, the ^{34}S-depletion is explained by mixing of SO_4^{2-} with high-$\delta^{34}S_{SO4}$ values from the upper section of the catchment with SO_4^{2-} with low-$\delta^{34}S_{SO4}$ values from tributaries 1, 2, and 3.

In contrast to the U-shaped valleys, the cross sections of tributary 1 (Fig. 7I), tributary 2 (Fig. 7J), and tributary 3 (Fig. 7K) displayed evidence for fluvial bedrock incision. For tributary 1, the river topographic profile was very steep (Fig. 9), and the valley was strongly V-shaped (Figs. 7I, 8A, 8F), suggesting fluvial incision into bedrock. For tributary 3 (Fig. 8K), the V-shaped portion of the profile was occasionally within a larger U-shaped cross section, indicative of fluvial incision following the glacial carving of the valley (Montgomery and Korup, 2011), and there was a prominent bedrock knickzone in the lower portion of the valley. Satellite imagery and field photography showed that the V-shaped valley walls have some landslide scarring and deposits that extend to the valley floor, indicating active bedrock erosion and delivery of rock to the riverbed (Appendix A, Fig. A.3). Within these incising reaches, $\delta^{34}S_{SO4}$ values indicated that SO_4^{2-} was dominantly sourced from fresh basalt, a pattern consistent with exposure of fresh minerals as the rivers erode into unweathered bedrock. Overall, lower $\delta^{34}S_{SO4}$ values were associated with higher fractions of V-shaped cross sections (Fig. 8K) and lower power law exponents (Fig. 8L; Appendix F, Fig. F.1); these observations partially led us to conclude that landscape morphology exerted the primary control on dissolved $\delta^{34}S_{SO4}$.

Above their knickzones, the upper mainstem valley and tributary 3 had similar elevation profiles (Fig. 9) and drainage areas, raising the question of why the two valleys had different cross-sectional geometries. Our results suggested, despite that Iceland was covered by an ice sheet during the last glacial maximum (Gudmundsson, 1997), that tributary 3 and the other V-shaped valleys were not shaped by glaciers to the same degree as the main valley. The orientation of the primary U-shaped valley in the Efri Haukadalsá catchment was interpreted to show ice flow was locally to the southwest, whereas some of the V-shaped tributaries were approximately orthogonal to this direction (Fig. 7). We proposed that the orientation of the V-shaped fluvial valleys sheltered them from ice flow and led to the preservation of their shape despite glaciation (Montgomery and Korup, 2011; Lajeunesse, 2014). Following deglaciation, these valleys maintained their steep valley walls and bedrock floors, allowing for continued bedrock incision and hillslope-channel coupling. In contrast, we interpreted that the valleys oriented parallel to the ice flow experienced major glacial erosion and were cut down such that less eroded tributaries became hanging tributaries (Fig. 9) (MacGregor et al., 2000). The low valley-floor gradients and undulating bedrock topography

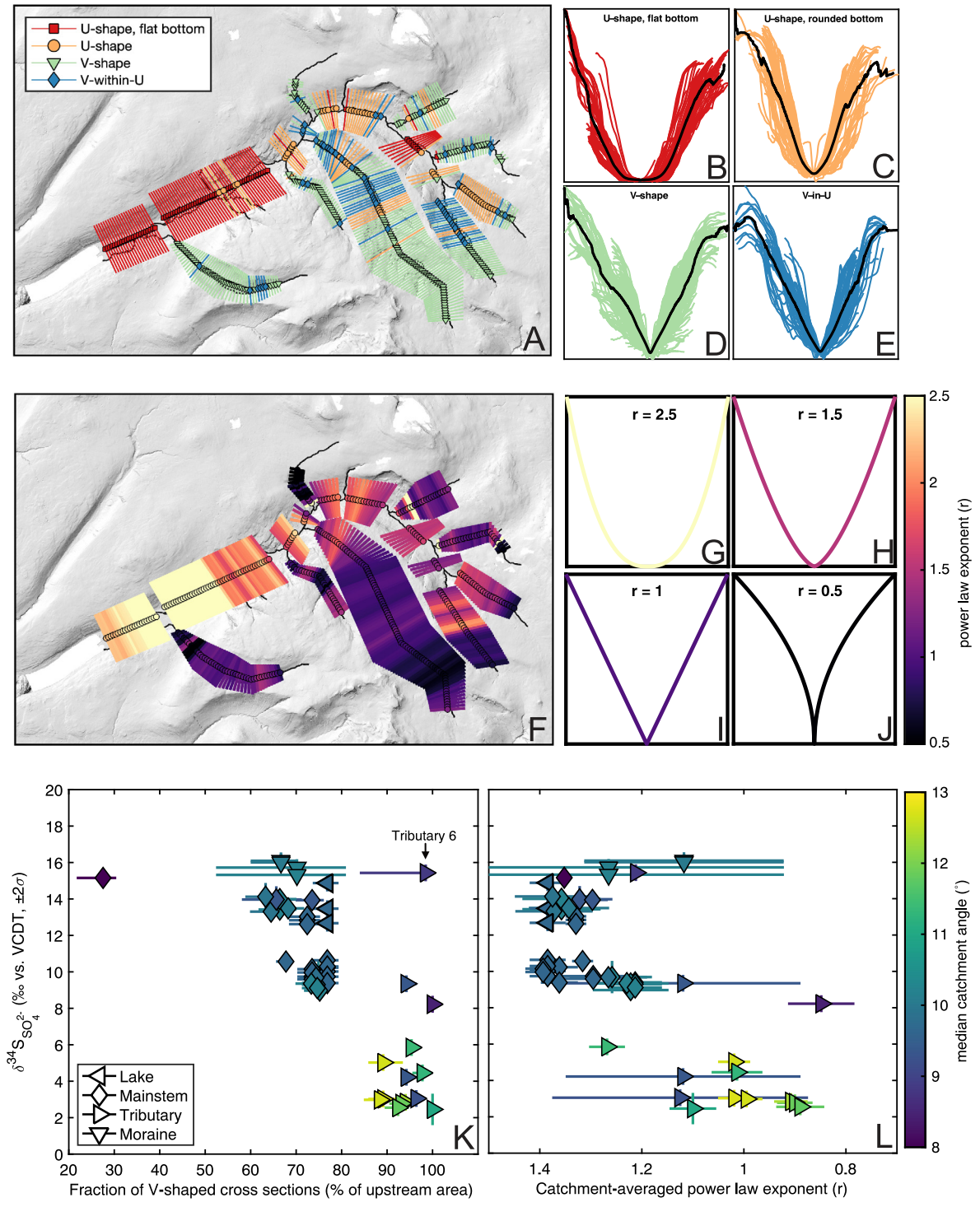

Fig. 8. Geomorphic analyses. (A) Each of 405 cross sections generated throughout the Efri Haukadalsá catchment was visually inspected and assigned into one of five groups: U-shaped with flat bottom, U-shaped, V-shaped, V-within-U shaped, and N/A. (B) Aligned and averaged cross sections identified as U-shaped with flat bottom (C) U-shaped with rounded bottom, (D) V-shaped, and (E) V-in-U shaped. Results in (A) through (E) are plotted for one of three rounds of manual classification, all of which yielded similar spatial distributions of cross section geometry and averaged elevation profiles. (F) Power law exponent fitted to each cross section, with examples for four different values of the shape parameter r: (G) 2.5, (H) 1.5, (I) 1, (J) 0.5 (Allen et al., 2018). (K) Values of $\delta^{34}S_{SO4}$ against the fraction of V-shaped cross sections in each catchment, color-coded by median catchment angle. Error bars indicate the minimum and maximum fraction of V-shaped cross sections in each catchment across the three rounds of manual identification, and accounting for cross sections characterized as N/A. Overall, results indicated lower values of $\delta^{34}S_{SO4}$ in samples with higher fractions of V-shaped cross sections upstream of the sampling site. The sample from tributary 6 was notable for having a high $\delta^{34}S_{SO4}$ value despite its upstream region being dominated by V-shaped cross sections. (L) Values of $\delta^{34}S_{SO4}$ against the average power law exponent r upstream of each sampling site. Error bars indicate the range in power law exponent calculated for two different treatments of the elevation data. Again, lower values of $\delta^{34}S_{SO4}$ were associated with V-shaped upstream cross sections.

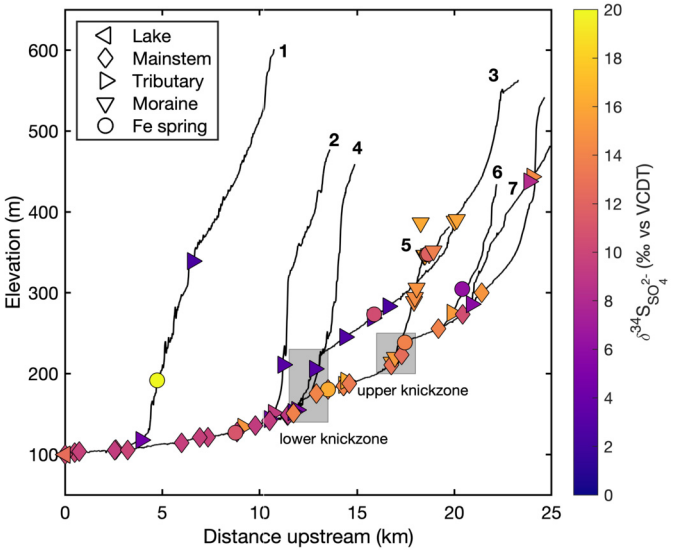

Fig. 9. River channel long profile with water samples coded by sample type and $\delta^{34}S_{SO4}$ value. The lower knickzone occurred near the confluence with tributary 3, and the upper knickzone occurred near confluence with tributary 5. The given numbers indicate tributary numbers (Fig. 2C).

with overdeepenings are typical of glacial valleys (MacGregor et al., 2000), and this disequilibrium with the fluvial system has led to interglacial fluvial and lacustrine aggradation, wide and flat valley floors, and a disconnect between bedrock sources and fluvial transport and weathering (Church and Ryder, 1972).

The physical abrasion associated with glacial erosion generates fine-grained sediment susceptible to rapid weathering (Vance et al., 2009). In a granitic landscape, the initial weathering pulse from deglaciation was previously shown to source strontium with elevated $^{87}Sr/^{86}Sr$ isotope ratios (Blum and Erel, 1995). Using a similar argument, the deglaciation at ~10 ka is expected to have generated large quantities of fine-grained sediment with fresh surface area throughout western Iceland, as evidenced by the moraine at tributary 5. In the short-term, weathering of such material could generate low-$\delta^{34}S_{SO4}$ values due to FeS_2 oxidation. However, values of $\delta^{34}S_{SO4}$ in water samples near the moraine in the catchment of the Efri Haukadalsá were elevated from that of unweathered bedrock and dominantly reflected SO_4^{2-} inputs from seasonal precipitation (Fig. 7). This observation suggested that FeS_2 in this fine-grained glacial sediment had already undergone oxidation in less than 10 kyr, which is comparable to the timescale for decay of the $^{87}Sr/^{86}Sr$ ratio sourced from glacial granitoid soils (Blum and Erel, 1995). Overall, when considering controls on $\delta^{34}S_{SO4}$ values and the role of glaciation in supplying FeS_2 for oxidative weathering, it was thus useful to consider the role of fluvial alluviation in disconnecting bedrock sources in formerly glaciated valleys, the persistence of some V-shaped valleys that maintain active bedrock incision, and the prior weathering of existing deposits such as moraines.

4.3. Relative abundance and isotopic ramifications of organic sulfur phases

We calculated the relative flux of organic and inorganic sulfur in two ways; the first method was based on observed carbon fluxes, and the second on sediment accumulation rate. Measurements of carbon concentration in suspended sediment ranged from 40 µg/L to 300 µg/L, with a mean value of 120 ± 90 µg/L (n = 11) (Torres et al., 2020). Using a C/S mass ratio of 35, the mean value we measured in deposit samples, and taking a characteristic river $[SO_4^{2-}]$ of 10 µM, the flux of organic sulfur in the Efri Haukadalsá was calculated as 1.1±1.6% (2σ) of the dissolved SO_4^{2-} flux. However, this estimate was biased to low values because our sampling was during summer when the river stage was relatively low and particle transport is expected to have been similarly low.

The second calculation relied on observations from the Haukadalsvatn sediment core (Geirsdóttir et al., 2009). Using a sediment accumulation rate of 5280 m^3/yr (Torres et al., 2020), a sediment density of 2 g/cm^3, a C/S mass ratio of 35, and an organic carbon fraction of 2 wt.% (Geirsdóttir et al., 2009), we calculated that 1.9×10^5 moles of S_{org} were transported annually as river suspended load. Taking river $[SO_4^{2-}]$ equal to 10 µM and scaling by discharge, we calculated that 4.3% of the sulfur flux occurred within organic phases. It is likely that this estimate was also biased to lower values by not accounting for the storage of particulate sulfur within the floodplain. While the magnitude of this underestimate is subject to assumption of porosity, sediment stored within the catchment could be 2–3 times the mass stored in the lake (Torres et al., 2020). On the basis of these two calculations, we concluded that flux of S_{org} in the Efri Haukadalsá was less than ~10% of the dissolved SO_4^{2-} flux. Globally, approximately 6% of non-anthropogenic river sulfur occurs within organic phases; the relative flux of S_{org} in the Efri Haukadalsá was thus comparable to the global value despite the lack of sedimentary lithologies in the catchment (Galy et al., 2015; Burke et al., 2018).

The removal of 10% SO_4^{2-} to organic phases could have exerted an influence on the Cl^-/SO_4^{2-} ratio of river water and, if removed through a fractionating process, dissolved $\delta^{34}S_{SO4}$. As a simple model, we considered whether or not the Cl^-/SO_4^{2-} and $\delta^{34}S_{SO4}$ of river water samples could reflect mixing of basalt and annually-integrated precipitation followed by fractional consumption according to a Rayleigh model (Appendix J, Fig. J.1). For this calculation we optimized for the end-member mixing fraction and isotope fractionation that best fit observations under the assumption that 10% of initial SO_4^{2-} was consumed, and then calculated the $\delta^{34}S$ of the reaction product. Although the calculated isotope fractionations were dependent on the choice of precipitation end-member, for most samples the required fractionation was more positive than expected for MSR (Appendix J, Fig. J.1). Moreover, for isotope effects offset from zero but elevated from MSR expectations, the product sulfur would have a median $\delta^{34}S$ value much lower than measured sediment $\delta^{34}S$ values (Fig. 5; Appendix J, Fig. J.1). These calculations thus indicated that, for the range in sediment $\delta^{34}S$ to largely match river water $\delta^{34}S_{SO4}$, the generation of S_{org} occurred with minimal sulfur isotope fractionation.

The overall assimilation of SO_4^{2-} by plants has a fractionation of only about 1.5‰ (Trust and Fry, 1992), although plant metabolites exhibit substantial isotopic variations (Tcherkez and Tea, 2013). Our results were consistent with this magnitude of fractionation and led us to conclude that the observed S_{org} phases were generated through SO_4^{2-} assimilation and subsequent reduction within biomass. These findings were largely consistent with those of Yi-Balan et al. (2014), who identified only a moderate offset in the $\delta^{34}S$ of organic biomass from SO_4^{2-} inputs in the Luquillo Critical Zone Observatory. Moreover, in previous work Zhu et al. (2016) found that the isotopic composition of humic acids extracted from Yangtze River sediment were similar to dissolved $\delta^{34}S_{SO4}$. Our results indicated that the sulfur isotopic composition of particles deposited in river catchments may, in general, not be systematically offset from river $\delta^{34}S_{SO4}$ values. Notably, this hypothesis should be further tested in tropical rivers with elevated organic carbon loading.

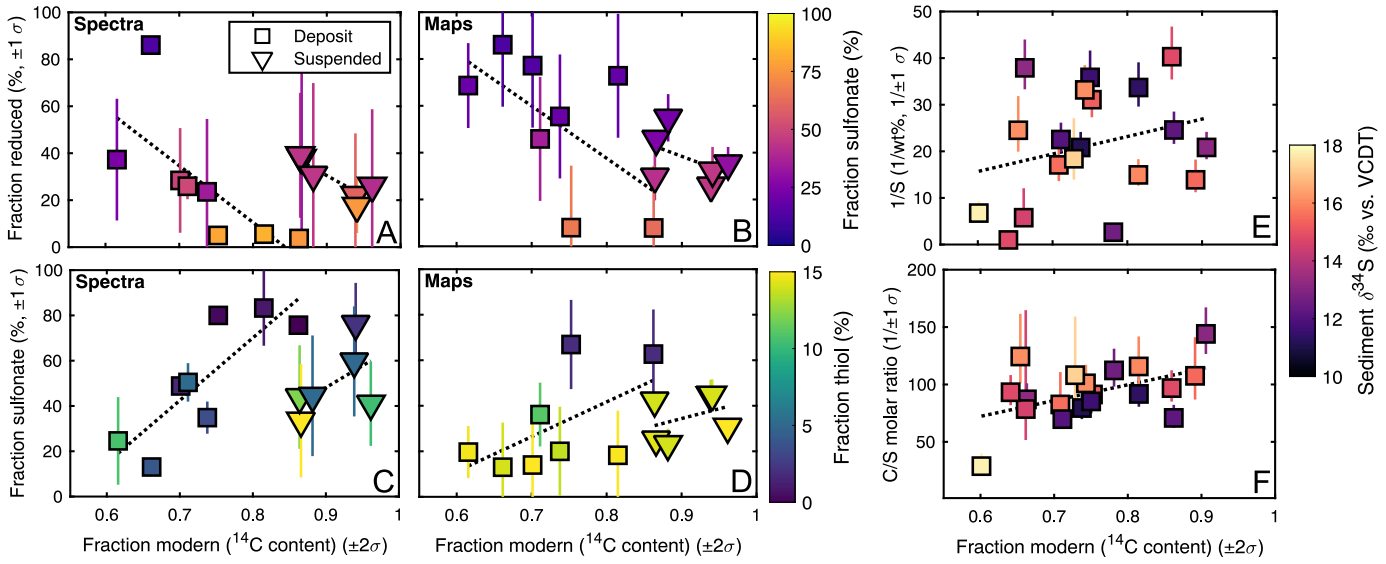

Fig. 10. Relationships among fitted spectroscopic data, fraction modern (^{14}C content), 1/S and C/S ratios, and sediment δ^{34}S. (A) $F_{reduced}$ (the sum of fractional contributions from disulfide, thiol, and sulfoxide speciation) derived from X-ray absorption spectra and from (B) multiple-energy maps against fraction modern, shape-coded as deposit samples (squares) or suspended sediment (triangles) and color-coded by the fractional contribution of sulfonate. Within each sample type, lower fraction modern was associated with more reduced speciation and a lower contribution of sulfonate. (C) Fractional contribution of sulfonate against fraction modern, from X-ray absorption spectra and from (D) multiple energy maps, color-coded by the fractional contribution of thiols. Within each sample type, the lower fractional contribution from sulfonate with decreasing ^{14}C content was related to increasing fractional contribution of thiols. Note that changes in the relative contributions of moieties are not independent due to the unit-sum constraint of our fitting; decreases in the relative contribution of sulfonate must be balanced by increases in the fractional contribution of other moieties, even if all other moieties have the same absolute contributions. (E) 1/S and (F) C/S molar ratio against fraction modern, color-coded by δ^{34}S. Sediment ^{14}C content was only weakly related with 1/S or C/S ratio. In all panels the moraine sample from site LHSS-06 was out of plotting range and excluded from regression.

4.4. Sulfur cycling during floodplain storage

X-ray absorption spectra revealed a substantial range in the relative contributions of thiol, disulfide, sulfoxide, sulfonate, and sulfate to suspended sediment, deposit samples, and vegetation (Fig. 6C). On average, the fractional sum of contributions from reduced sulfur moieties ($F_{reduced}$) to deposit samples was similar between deposit samples stored within the floodplain (25.1 ± 51.6%, 2σ) and sediment suspended in the river (28.9 ± 17.3%, 2σ). One sample from LHSS-07 at 25 cm depth, a horizon with elevated organic carbon content, appeared as an outlier from other deposit samples by showing a large contribution from disulfide (Fig. 6). Moreover, multiple-energy maps indicated that a wide diversity of sulfur speciation was present across spatial scales (Torres et al., 2020). These observations were consistent with prior observations of organic sulfur phases within natural soils (Xia et al., 1998; Solomon et al., 2011; Prietzel et al., 2011).

The mean $F_{reduced}$ value in vegetation samples, as derived from spectra, was 56.2 ± 16.8% (2σ). This value was consistent with results of Jalilehvand (2005), who measured X-ray absorption spectra at the sulfur K-edge on plant leaves from northern California. Redox imaging of photosynthetic tissues of grasses and sedges from the Efri Haukadalsá catchment identified spatial diversity in sulfur speciation. For example, the outer photosynthetic mesophyll tissue of sample LHVS19-01 was S-rich and relatively reduced, while the inner parts richer in vasculature were lower in sulfur content and more oxidized (Appendix C, Fig. C.1).

The relative abundances of disulfide, sulfoxide, and sulfate were similar across suspended sediment, deposit samples, and vegetation (Fig. 6D). However, large changes were identified in the relative contributions of thiol and sulfonate moieties between the different materials. Thiols were abundant in vegetation, while sulfonate moieties were rare. Conversely, suspended sediment and deposit samples displayed abundant sulfonate but only a small contribution from thiols. Prior studies have observed a similar abundance of sulfonate species in soils, suggesting it is a recalcitrant form of organic sulfur capable of resisting long-term oxidation compared to more reactive species (Autry and Fitzgerald, 1990; Solomon et al., 2011).

If S_{org} in deposit and suspended sediment was mostly derived from plant material, as suggested by the similarity of sediment δ^{34}S and dissolved $\delta^{34}S_{SO4}$, our observations indicated that the processes of generating, transporting, and storing sediment involved net conversion of thiols into sulfonates. However, we did not recover a positive relationship between ^{14}C abundance in sediment and the fractional contribution of reduced moieties to X-ray absorption spectra (Fig. 10). For both deposit and suspended samples, older sediment was associated with higher $F_{reduced}$ values (Figs. 10A, B) and a lower fractional contribution from sulfonate specifically (Figs. 10C, D), patterns opposite of expectations if the aging process generated sulfonate from thiol.

Boye et al. (2017) suggested that carbon-bearing phases with redox states above a thermodynamic threshold were preferentially oxidized within anaerobic settings while reduced carbon-bearing phases were preferentially stored in floodplains. Our data displayed older ^{14}C ages associated with carbon that had a more reduced organic sulfur speciation in sediment (Fig. 10) and suggested that a similar explanation may pertain to our sulfur observations. In this case, the oxidized phases such as sulfonate would have been preferentially lost from the floodplain. We observed that the 1/S and C/S ratios of samples were not clearly correlated with ^{14}C age, suggesting that, under this interpretation, carbon and sulfur would have been preferentially oxidized at similar rates through time (Fig. 10E, F). However, because the radiocarbon content of sediment reflects a complex mixture of time-dependent physical reworking processes and the addition of newly fixed C_{org}, we stress that ^{14}C content only approximately represents deposit age (Torres et al., 2017, 2020).

5. Conclusions

We have studied the major ion chemistry, $\delta^{34}S_{SO4}$, and speciation of sulfur in river water, sediment, and vegetation samples from the Efri Haukadalsá catchment of western Iceland, as well as the dissolved chemistry of river water samples from around NW Iceland and the Hvítá catchment. We found that dissolved anion chemistry reflected mixing of products generated from basalt weathering and seasonal precipitation, while dissolved cation chemistry also reflected influences of clay formation. In the catchment of the Efri Haukadalsá, fluxes of organic sulfur in suspended sediment constituted less than approximately 10% of the dissolved flux of SO_4^{2-}. X-ray absorption spectroscopy of suspended sediment, deposit samples, and vegetation identified a range of reduced sulfur compounds, with sediment enriched in sulfonate and depleted in thiol relative to vegetation. Because the $\delta^{34}S$ of deposit samples was similar to that of dissolved SO_4^{2-}, we concluded that organic phases did not require formation through MSR and more likely were generated through SO_4^{2-} assimilation and reduction within biomass. Overall, biological processes exerted only a minimal influence on $\delta^{34}S_{SO4}$ values in the Efri Haukadalsá. Rather, landscape morphology exerted the primary control on the $^{34}S/^{32}S$ ratio of river SO_4^{2-}. Glacially eroded, U-shaped valleys with bedrock floor overdeepenings that have been partially or completely filled through fluvial sedimentation lacked fresh bedrock exposure and had $\delta^{34}S_{SO4}$ values reflecting meteoric inputs. In contrast, V-shaped valleys had lower $\delta^{34}S_{SO4}$ values reflecting the continued exposure and weathering of fresh bedrock. We interpreted these differences in valley shape, alluviation, and $\delta^{34}S_{SO4}$ as reflecting contrasting patterns of ice-flow and development of fluvial drainage networks resulting from topographic disequilibrium across glacial-interglacial cycles. Overall, our results emphasized the tight linkages between pyrite oxidation and geomorphic processes. This work has indicated that, even in the presence of organic sulfur fluxes, inversion models of dissolved river chemistry can be used to reconstruct the fractional contributions of lithologic end-members to river SO_4^{2-}. This research thus validated the application of river inversion models for constraining the impact of pyrite oxidation on the global carbon cycle.

6. Data statement

Data from this article on major ion concentrations, river water and precipitation $\delta^{34}S_{SO4}$ values, sediment $\delta^{34}S$ and $F_{reduced}$ values, and vegetation $F_{reduced}$ values are available as Supplementary material.

CRediT authorship contribution statement

Preston C. Kemeny: Conceptualization, Formal analysis, Investigation, Project administration, Software, Visualization, Writing – original draft. **Mark A. Torres:** Conceptualization, Funding acquisition, Investigation, Project administration, Supervision, Writing – review & editing. **Michael P. Lamb:** Funding acquisition, Supervision, Writing – review & editing. **Samuel M. Webb:** Resources, Writing – review & editing. **Nathan Dalleska:** Resources, Writing – review & editing. **Trevor Cole:** Investigation, Writing – review & editing. **Yi Hou:** Investigation. **Jared Marske:** Writing – review & editing. **Jess F. Adkins:** Funding acquisition, Resources, Supervision, Writing – review & editing. **Woodward W. Fischer:** Conceptualization, Funding acquisition, Resources, Supervision, Writing – review & editing.

Declaration of competing interest

The authors declare that they have no known competing financial interests or personal relationships that could have appeared to influence the work reported in this paper.

Acknowledgements

P.C.K. is supported by The Fannie and John Hertz Foundation Cohan-Jacobs and Stein Families Fellowship. This research was conducted with government support under and awarded by DoD, Air Force Office of Scientific Research, National Defense Science and Engineering Graduate (NDSEG) Fellowship, 32 CFR 168a (P.C.K.). M.A.T. gratefully acknowledges support from the Alfred P. Sloan Foundation. This research was supported by the Discovery Fund (to W.W.F. and M.P.L.) at the California Institute of Technology, and this work was partially support by the US National Science Foundation through grants 1349858 and 1834492. Use of the Stanford Synchrotron Radiation Lightsource, SLAC National Accelerator Laboratory, is supported by the U.S. Department of Energy, Office of Science, Office of Basic Energy Sciences under Contract No. DE-AC02-76SF00515. We acknowledge DEMs provided by the Polar Geospatial Center under NSF-OPP awards 1043681, 1559691, and 1542736. We gratefully acknowledge A.J. West for loaning sampling equipment, A. Sessions, F. Wu, and A. Phillips for assistance with EA-IRMS measurements, G. Lopez, T. Present, and D. Johnson for assistance with MC-ICP-MS measurements, N. Edwards, S. Bone, and C. Roach for assistance with synchrotron measurements at SLAC, and A. Phillips and P. Mateo for advice on figure design. We thank Louis Derry and two anonymous referees for their constructive comments.

Appendix. Supplementary material

Supplementary material related to this article can be found online at https://doi.org/10.1016/j.epsl.2021.116838.

References

Allen, G.H., Pavelsky, T.M., Barefoot, E.A., Lamb, M.P., Butman, D., Tashie, A., Gleason, C.J., 2018. Similarity of stream width distributions across headwater systems. Nat. Commun. 9 (1), 1–7. https://doi.org/10.1038/s41467-018-02991-w.

Andreae, M.O., Berresheim, H., Bingemer, H., Jacob, D.J., Lewis, B.L., Li, S.M., Talbot, R.W., 1990. The atmospheric sulfur cycle over the Amazon Basin: 2. Wet season. J. Geophys. Res., Atmos. 95 (D10), 16813–16824. https://doi.org/10.1029/JD095iD10p16813.

Autry, A.R., Fitzgerald, J.W., 1990. Sulfonate S: a major form of forest soil organic sulfur. Biol. Fertil. Soils 10 (1), 50–56. https://doi.org/10.1007/BF00336124.

Bern, C.R., Chadwick, O.A., Kendall, C., Pribil, M.J., 2015. Steep spatial gradients of volcanic and marine sulfur in Hawaiian rainfall and ecosystems. Sci. Total Environ. 514, 250–260. https://doi.org/10.1016/j.scitotenv.2015.02.001.

Blum, J.D., Erel, Y., 1995. A silicate weathering mechanism linking increases in marine $^{87}Sr/^{86}Sr$ with global glaciation. Nature 373 (6513), 415–418. https://doi.org/10.1038/373415a0.

Bohic, S., Murphy, K., Paulus, W., Cloetens, P., Salomé, M., Susini, J., Double, K., 2008. Intracellular chemical imaging of the developmental phases of human neuromelanin using synchrotron X-ray microspectroscopy. Anal. Chem. 80 (24), 9557–9566. https://doi.org/10.1021/ac801817k.

Boye, K., Noël, V., Tfaily, M.M., Bone, S.E., Williams, K.H., Bargar, J.R., Fendorf, S., 2017. Thermodynamically controlled preservation of organic carbon in floodplains. Nat. Geosci. 10, 415–419. https://doi.org/10.1038/ngeo2940.

Burke, A., Present, T.M., Paris, G., Rae, E.C., Sandilands, B.H., Gaillardet, J., Voss, B.M., 2018. Sulfur isotopes in rivers: insights into global weathering budgets, pyrite oxidation, and the modern sulfur cycle. Earth Planet. Sci. Lett. 496, 168–177. https://doi.org/10.1016/j.epsl.2018.05.022.

Calmels, D., Gaillardet, J., Brenot, A., France-Lanord, C., 2007. Sustained sulfide oxidation by physical erosion processes in the Mackenzie River basin: climatic perspectives. Geology 35 (11), 1003–1006. https://doi.org/10.1130/G24132A.1.

Church, M., Ryder, J.M., 1972. Paraglacial sedimentation: a consideration of fluvial processes conditioned by glaciation. Geol. Soc. Am. Bull. 83 (10), 3059–3072. https://doi.org/10.1130/0016-7606(1972)83[3059:PSACOF]2.0.CO;2.

Gaillardet, J., Dupré, B., Louvat, P., Allegre, C.J., 1999. Global silicate weathering and CO_2 consumption rates deduced from the chemistry of large rivers. Chem. Geol. 159 (1), 3–30. https://doi.org/10.1016/S0009-2541(99)00031-5.

Galy, V., Peucker-Ehrenbrink, B., Eglinton, T., 2015. Global carbon export from the terrestrial biosphere controlled by erosion. Nature 521 (7551), 204–207. https://doi.org/10.1038/nature14400.

Geirsdóttir, Á., Miller, G.H., Thordarson, T., Ólafsdóttir, K.B., 2009. A 2000 year record of climate variations reconstructed from Haukadalsvatn, West Iceland. J. Paleolimnol. 41 (1), 95–115. https://doi.org/10.1007/s10933-008-9253-z.

Gislason, S.R., Arnorsson, S., Armannsson, H., 1996. Chemical weathering of basalt in Southwest Iceland; effects of runoff, age of rocks and vegetative/glacial cover. Am. J. Sci. 296 (8), 837–907. https://doi.org/10.2475/ajs.296.8.837.

Gislason, S.R., Torssander, P., 2006. Response of sulfate concentration and isotope composition in Icelandic rivers to the decline in global atmospheric SO_2 emissions into the North Atlantic region. Environ. Sci. Technol. 40 (3), 680–686. https://doi.org/10.1021/es051325o.

Gudmundsson, H.J., 1997. A review of the Holocene environmental history of Iceland. Quat. Sci. Rev. 16 (1), 81–92. https://doi.org/10.1016/S0277-3791(96)00043-1.

Hemingway, J.D., Olson, H., Turchyn, A.V., Tipper, E.T., Bickle, M.J., Johnston, D.T., 2020. Triple oxygen isotope insight into terrestrial pyrite oxidation. Proc. Natl. Acad. Sci. USA 117 (14), 7650–7657. https://doi.org/10.1073/pnas.1917518117.

Hjartarson, Á., Sæmundsson, K., 2014. Geological Map of Iceland. Bedrock. 1:600 000. Iceland GeoSurvey.

Hildebrand, L.W., Torssander, P., 1998. Sulfur isotope ratios from the Katla Volcanic Centre—with implications for mantle heterogeneities. In: Water-Rock Interaction, pp. 451–454.

Jalilehvand, F., 2005. Sulfur speciation in intact plant leaves by XANES spectroscopy.

John, S.G., Adkins, J.F., 2010. Analysis of dissolved iron isotopes in seawater. Mar. Chem. 119 (1), 65–76. https://doi.org/10.1016/j.marchem.2010.01.001.

Johnson, J.E., Gerpheide, A., Lamb, M.P., Fischer, W.W., 2014. O_2 constraints from Paleoproterozoic detrital pyrite and uraninite. GSA Bull. 126 (5–6), 813–830. https://doi.org/10.1130/B30949.1.

Kemeny, P.C., Lopez, G.I., Dalleska, N.F., Torres, M., Burke, A., Bhatt, M.P., Adkins, J.F., 2020. Sulfate sulfur isotopes and major ion chemistry reveal that pyrite oxidation counteracts CO_2 drawdown from silicate weathering in the Langtang-Trisuli-Narayani River system, Nepal Himalaya. Geochim. Cosmochim. Acta 294, 43–69. https://doi.org/10.1016/j.gca.2020.11.009.

Kertesz, M.A., Mirleau, P., 2004. The role of soil microbes in plant sulphur nutrition. J. Exp. Bot. 55 (404), 1939–1945. https://doi.org/10.1093/jxb/erh176.

Kump, L.R., Garrels, R.M., 1986. Modeling atmospheric O_2 in the global sedimentary redox cycle. Am. J. Sci. 286 (5), 337–360. https://doi.org/10.2475/ajs.286.5.337.

Lajeunesse, P., 2014. Buried preglacial fluvial gorges and valleys preserved through Quaternary glaciations beneath the eastern Laurentide Ice Sheet. GSA Bull. 126 (3–4), 447–458. https://doi.org/10.1130/B30911.1.

MacGregor, K.R., Anderson, R.S., Anderson, S.P., Waddington, E.D., 2000. Numerical simulations of glacial-valley longitudinal profile evolution. Geology 28 (11), 1031–1034. https://doi.org/10.1130/0091-7613(2000)28<1031:NSOGLP>2.0.CO;2.

Manceau, A., Nagy, K.L., 2012. Quantitative analysis of sulfur functional groups in natural organic matter by XANES spectroscopy. Geochim. Cosmochim. Acta 99, 206–223. https://doi.org/10.1016/j.gca.2012.09.033.

Montgomery, D.R., Korup, O., 2011. Preservation of inner gorges through repeated Alpine glaciations. Nat. Geosci. 4 (1), 62–67. https://doi.org/10.1038/ngeo1030.

Moulton, K.L., West, J., Berner, R.A., 2000. Solute flux and mineral mass balance approaches to the quantification of plant effects on silicate weathering. Am. J. Sci. 300 (7), 539–570. https://doi.org/10.2475/ajs.300.7.539.

Paris, G., Sessions, A.L., Subhas, A.V., Adkins, J.F., 2013. MC-ICP-MS measurement of $\delta^{34}S$ and $\Delta^{33}S$ in small amounts of dissolved sulfate. Chem. Geol. 345, 50–61. https://doi.org/10.1016/j.chemgeo.2013.02.022.

Prietzel, J., Botzaki, A., Tyufekchieva, N., Brettholle, M., Thieme, J., Klysubun, W., 2011. Sulfur speciation in soil by S K-edge XANES spectroscopy: comparison of spectral deconvolution and linear combination fitting. Environ. Sci. Technol. 45 (7), 2878–2886. https://doi.org/10.1021/es102180a.

Robinson, Z.P., Fairchild, I.J., Spiro, B., 2009. The sulphur isotope and hydrochemical characteristics of Skeiðarársandur, Iceland: identification of solute sources and implications for weathering processes. Hydrol. Process., Int. J. 23 (15), 2212–2224. https://doi.org/10.1002/hyp.7368.

Sakai, H., Gunnlaugsson, E., Tomasson, J., Rouse, J.E., 1980. Sulfur isotope systematics in Icelandic geothermal systems and influence of seawater circulation at Reykjanes. Geochim. Cosmochim. Acta 44 (8), 1223–1231. https://doi.org/10.1016/0016-7037(80)90076-9.

Schwanghart, W., Kuhn, N.J., 2010. TopoToolbox: a set of Matlab functions for topographic analysis. Environ. Model. Softw. 25 (6), 770–781. https://doi.org/10.1016/j.envsoft.2009.12.002.

Sigvaldason, G.E., Óskarsson, N., 1976. Chlorine in basalts from Iceland. Geochim. Cosmochim. Acta 40 (7), 777–789. https://doi.org/10.1016/0016-7037(76)90030-2.

Solomon, D., Lehmann, J., de Zarruk, K.K., Dathe, J., Kinyangi, J., Liang, B., Machado, S., 2011. Speciation and long- and short-term molecular-level dynamics of soil organic sulfur studied by X-ray absorption near-edge structure spectroscopy. J. Environ. Qual. 40 (3), 704–718. https://doi.org/10.2134/jeq2010.0061.

Stefánsson, A., Keller, N.S., Robin, J.G., Ono, S., 2015. Multiple sulfur isotope systematics of Icelandic geothermal fluids and the source and reactions of sulfur in volcanic geothermal systems at divergent plate boundaries. Geochim. Cosmochim. Acta 165, 307–323. https://doi.org/10.1016/j.gca.2015.05.045.

Tcherkez, G., Tea, I., 2013. $^{32}S/^{34}S$ isotope fractionation in plant sulphur metabolism. New Phytol. 200 (1), 44–53. https://doi.org/10.1111/nph.12314.

Thorpe, M.T., Hurowitz, J.A., Dehouck, E., 2019. Sediment geochemistry and mineralogy from a glacial terrain river system in southwest Iceland. Geochim. Cosmochim. Acta 263, 140–166. https://doi.org/10.1016/j.gca.2019.08.003.

Torres, M.A., West, A.J., Li, G., 2014. Sulphide oxidation and carbonate dissolution as a source of CO_2 over geological timescales. Nature 507 (7492), 346–349. https://doi.org/10.1038/nature13030.

Torres, M.A., West, A.J., Clark, K.E., Paris, G., Bouchez, J., Ponton, C., et al., 2016. The acid and alkalinity budgets of weathering in the Andes–Amazon system: insights into the erosional control of global biogeochemical cycles. Earth Planet. Sci. Lett. 450, 381–391. https://doi.org/10.1016/j.epsl.2016.06.012.

Torres, M.A., Limaye, A.B., Ganti, V., Lamb, M.P., West, A.J., Fischer, W.W., 2017. Model predictions of long-lived storage of organic carbon in river deposits. Earth Surf. Dyn. 5 (4), 711–730. https://doi.org/10.5194/esurf-5-711-2017.

Torres, M.A., Kemeny, P.C., Lamb, M.P., Cole, T.L., Fischer, W.W., 2020. Long-term storage and age-biased export of fluvial organic carbon: field evidence from West Iceland. Geochem. Geophys. Geosyst. https://doi.org/10.1029/2019GC008632.

Torssander, P., 1989. Sulfur isotope ratios of Icelandic rocks. Contrib. Mineral. Petrol. 102 (1), 18–23. https://doi.org/10.1007/BF01160187.

Trust, B.A., Fry, B., 1992. Stable sulphur isotopes in plants: a review. Plant Cell Environ. 15 (9), 1105–1110. https://doi.org/10.1111/j.1365-3040.1992.tb01661.x.

Turchyn, A.V., Tipper, E.T., Galy, A., Lo, J.K., Bickle, M.J., 2013. Isotope evidence for secondary sulfide precipitation along the Marsyandi River, Nepal, Himalayas. Earth Planet. Sci. Lett. 374, 36–46. https://doi.org/10.1016/j.epsl.2013.04.033.

Vance, D., Teagle, D.A., Foster, G.L., 2009. Variable Quaternary chemical weathering fluxes and imbalances in marine geochemical budgets. Nature 458 (7237), 493–496. https://doi.org/10.1038/nature07828.

Walker, J.C.G., Hays, P.B., Kasting, J.F., 1981. A negative feedback mechanism for the long-term stabilization of Earth's surface temperature. J. Geophys. Res. 86, 9776–9782. https://doi.org/10.1029/JC086iC10p09776.

Webb, S.M., 2005. SIXpack: a graphical user interface for XAS analysis using IFEFFIT. Phys. Scr. 2005 (T115), 1011.

Webb, S.M., 2011. The MicroAnalysis Toolkit: X-ray fluorescence image processing software. In: AIP Conference Proceedings (Vol. 1365, No. 1). American Institute of Physics, pp. 196–199.

Xia, K., Weesner, F., Bleam, W.F., Helmke, P.A., Bloom, P.R., Skyllberg, U.L., 1998. XANES studies of oxidation states of sulfur in aquatic and soil humic substances. Soil Sci. Soc. Am. J. 62 (5), 1240–1246. https://doi.org/10.2136/sssaj1998.03615995006200050014x.

Yi-Balan, A.S., Amundson, R., Buss, H.L., 2014. Decoupling of sulfur and nitrogen cycling due to biotic processes in a tropical rainforest. Geochim. Cosmochim. Acta 142, 411–428. https://doi.org/10.1016/j.gca.2014.05.049.

Zhu, M.X., Chen, L.J., Yang, G.P., Huang, X.L., Zhao, Y.D., 2016. Composition of organic sulfur in riverine and marine sediments: insights from sulfur stable isotopes and XANES spectroscopy. Org. Geochem. 99, 102–112. https://doi.org/10.1016/j.orggeochem.2016.07.002.